Journal of Materials Chemistry A

Performance Enhancement Strategies of Surface Plasmon Resonance Sensors in Direct Glucose Detection using Pristine and Modified UiO-66: Effects of Morphology, Immobilization Technique, and Signal Amplification

Journal:	*Journal of Materials Chemistry A*
Manuscript ID	TA-ART-10-2021-008741.R1
Article Type:	Paper
Date Submitted by the Author:	29-Dec-2021
Complete List of Authors:	Gumilar, Gilang; Bandung Institute of Technology, Engineering Physics Henzie, Joel; National Institute for Materials Science, International Center for Materials Nanoarchitectonics (WPI-MANA) Yuliarto, Brian; Institut Teknologi Bandung, Advanced Functional Materials Research Group; Institut Teknologi Bandung, Research Center for Nanoscience and Nanotechnology Patah, Aep; Institut Teknologi Bandung, Inorganic & Physical Chemistry Nugraha, Nugraha; Institut Teknologi Bandung, Engineering Physics Iqbal, Muhammad; Institut Teknologi Bandung, Advanced Functional Materials Research Group A. Amin, Mohammed ; Taif University, ; Taif University, Saudi Arabia Hossain, Md.; University of Queensland, School of Mechanical and Mining Engineering Yamauchi, Yusuke; University of Queensland, School of Chem Eng and AIBN Kaneti, Yusuf; The University of Queensland, Australian Institute for Bioengineering and Nanotechnology

Performance Enhancement Strategies of Surface Plasmon Resonance Sensors in Direct Glucose Detection using Pristine and Modified UiO-66: Effects of Morphology, Immobilization Technique, and Signal Amplification

Gilang Gumilar[1,2], Joel Henzie[3], Brian Yuliarto[2,4]*, Aep Patah[5], Nugraha Nugraha[2,4], Muhammad Iqbal[2,3], Mohammed A. Amin[6,] Md. Shariar A. Hossain[7,8], Yusuke Yamauchi[3,8], Yusuf Valentino Kaneti[8]**

[1] *Welding and Fabrication Engineering Technology Department, Institut Teknologi Sains Bandung, Central Cikarang, Bekasi 17530, Indonesia*

[2] *Advanced Functional Materials (AFM) Laboratory, Engineering Physics Department, Institut Teknologi Bandung, Bandung 40132, Indonesia*

[3] *JST-ERATO Yamauchi Materials Space-Tectonics Project and International Center for Materials Nanoarchitectonics (WPI-MANA), National Institute for Materials Science (NIMS), 1-1 Namiki, Tsukuba, Ibaraki 305-0044, Japan*

[4] *Research Center for Nanoscience and Nanotechnology (RCNN), Institut Teknologi Bandung, Bandung 40132, Indonesia*

[5] *Inorganic & Physical Chemistry Research Division, Institut Teknologi Bandung, Bandung 40132, Indonesia*

[6] *Department of Chemistry, College of Science, Taif University, P. O. Box 11099, Taif 21194, Saudi Arabia*

[7] *School of Mechanical and Mining Engineering, The University of Queensland, St. Lucia, QLD 4067, Australia*

[8] *School of Chemical Engineering and Australian Institute for Bioengineering and Nanotechnology (AIBN), The University of Queensland, St. Lucia, QLD 4072, Australia*

E-mails: gilang.gumilar@itsb.ac.id; brian@tf.itb.ac.id; v.kaneti@uq.edu.au

Abstract

Diabetes is a dangerous disease caused by the inability of the body to produce and use insulin properly, resulting in the increase in blood glucose level. The most advanced technology for glucose detection is the surface plasmon resonance (SPR)-based sensor. However, this technology has a slight drawback due to the small size of glucose. As a porous material, the Zr-based MOF, UiO-66, has a good adsorption to glucose through hydrogen bonding, so it can be utilized as a receptor and active layer for the SPR glucose sensor, without the need for other receptors, such as glucose oxidase, concanavalin A, or boronic acid-based compounds. This study investigates the morphology effect, immobilization techniques, and signal amplification strategies for optimizing the utilization of UiO-66 in SPR glucose sensor. By optimizing these parameters, a high-performance SPR glucose sensor with a detection limit of 0.0693 mM (S/N = 3) in the concentration range of 0.01-10 mM is successfully developed. In addition, the selectivity test reveals that the UiO-66/Au-based SPR sensor exhibits a high selectivity toward glucose. Furthermore, the developed SPR sensor showed good ability for detecting glucose in human blood serum, suggesting its promising potential for practical applications.

Keywords: SPR glucose sensor; Metal-organic frameworks; Au nanoparticles, Morphology effect, Immobilization effect; Signal amplification.

1. Introduction

Surface plasmon resonance (SPR) technology is commonly used as a tool to observe the molecular interactions between analytes in real-time, thus allowing it to be used as a sensor.[1,2] Although this technology promises rapid measurement, high sensitivity, high selectivity, and label-

free detection, it struggles to detect molecules with molecular weights of less than 200 Da.[3] Therefore, glucose with a molecular weight of 180 Da is quite difficult to detect by this technology, even though blood glucose level is widely used to diagnose diabetes.[4,5] Due to the deadly nature of this disease, the performance of SPR sensor for glucose detection needs to be improved so that its advantages can be utilized properly.

Several studies have attempted to solve the limitations of SPR technology for glucose detection. The most widely used approach is to develop a glucose receptor. The most commonly used receptor is glucose oxidase but it is strongly influenced by pH, and temperature, and its activity decreases with increasing measurement time, thus affecting the signal readings.[6,7] Other receptors which have been used include boronic acid-based compounds, glucose/galactose binding protein (GGBP), and concanavalin A (Con A). All three receptors can bind well to glucose to increase the selectivity and sensitivity of the SPR sensor. However, boronic acid-based compounds depend on pH, while GGBP needs genetic engineering and labeling for high concentrations, and Con A is toxic.[4,6,8,9] The second most used approach is to use a host matrix as an anchoring site for glucose receptors. In addition, the host matrix can also protect the receptors from harsh environments, collect analyte targets, and promote electron transport. Singh *et al.* deposited ZnO as an active layer on gold discs and immobilized it with GO_x to detect glucose.[10] They observed an increase in sensitivity due to the availability of oxygen defects on the surface and good electron transfer between Au and ZnO. Another study demonstrated that the GO_x encapsulation by ZIF-8 could protect GO_x and increase the glucose adsorption.[11] Although the combination of the receptor with the host matrix shows good performance, the immobilization process on the surface of the SPR sensor chip is not easy to perform.

Metal-organic frameworks (MOFs) as porous crystalline materials have the potential to be used as active layers on SPR chips for direct glucose detection without the use of additional receptors. This is because MOFs have high surface areas, tunable pore structures, and easy functionalization.[12,13] Because of this, MOFs have been extensively researched in various other applications, such as separation technology,[13–15] gas storage,[16] energy,[17,18] catalysis,[19,20] and antibacterial agents.[21,22] For instance, Zeng *et al.* compared the performance of ZIF-8 (Zn), UiO-66 (Zr), MIL-100 (Fe), MIL-96 (Al), MIL-101 (Cr), MIL-100 (Cr), and MIL-53 (Cr) to separate fructose and glucose.[23] They demonstrated the higher adsorption ability and selectivity of UiO-66 compared to these other MOFs to fructose and glucose due to the increased presence of active O-H groups that could bind to the O-H group in glucose. UiO-66 is a metal-organic framework (MOF)

which is composed of Zr as the metal center and 1,4-benzene dicarboxylate as the organic linker. It possesses a number of attractive characteristics, including large specific surface area, high thermal stability, and good chemical stability.[14,24,25] These advantages make it a good candidate as a receptor and an active material in direct detection of glucose using SPR technology. Several other MOFs have also been used in SPR sensors. Hang and co-workers employed Au@MIL-100(Fe) core-shell to detect glucose with the SPR technique without using enzymes but using 3-aminophenyl boronic acid hemisulfate (PBA).[26] This core-shell MOF exhibited a significant response in the 0-12 mM range, however the LOD is limited to 12 mM. Zhu *et al.* used ZIF-8 to encapsulate GO_x and the resulting GO_x@ZIF-8 sensor was capable of detecting low glucose concentrations between 1 to 8 mM.[11] However, both sensors still required glucose receptors, and only effective for detecting high glucose concentrations. Therefore, it is important to develop MOF-based SPR sensors which are sensitive, selective and have low LOD without the use of enzymes and specific glucose receptors.

To address the above challenges, several strategies have been proposed. The first is to optimize the adsorption capacity and therefore, the sensitivity of the SPR biosensor by optimizing the surface area of the active material.[27] Generally, the larger the surface area, the greater the adsorption capacity and sensitivity.[28] This strategy was demonstrated by several researchers and was successful in improving the performance of SPR biosensors. For example, Mudgal *et al.* used graphene to enlarge the surface area of the SPR active layer composed of $BaTiO_3$-graphene-top affinity layer to detect Pseudomonas bacteria.[29] Samavati and co-workers hybridized Ag with large surface area ZnO to enhance the saline detection.[30]

The second strategy is to optimize the method of immobilization. Huang *et al.* investigated the effect of the MOFs thin film fabrication method on the optical properties, namely the refractive index of the film.[31] The refractive index is an important parameter in the SPR biosensor technique because the surface polariton propagation is highly dependent on this parameter.[32] Therefore, the immobilization technique can influence the SPR sensor performance. In addition, the surface roughness due to the immobilization technique also affects the homogeneity of the biomolecule adsorption, and therefore, the number of active sites that can be accessed by biomolecules.[31,33–35] Agarwal *et al.* studied the effect of modified Ti/Ag deposition/immobilization techniques onto indium tin oxide (ITO) substrate toward the surface roughness of the SPR sensor for sucrose detection.[36] They found that the rougher the surface, the lower the sensitivity of the sensor. This study indicates the importance of paying attention to immobilization techniques.

The next strategy is to amplify the SPR signal in the sensor system using the plasmonic properties of localized surface plasmonic resonance (LSPR) of Au nanoparticles (AuNp).[37–42] Wu and co-workers demonstrated that the DNAzyme-AuNp conjugation immobilized on the SPR sensor could reduce the LOD by two or three orders in the detection of Pb^{2+} ions in water.[38] Kaczmarczyk *et al.* achieved signal amplification by conjugating antibodies with AuNp to detect aflatoxin M1 in milk with a low LOD of 18 pg/mL.[37] Further, Akgönüllü *et al.* reported that polymer hybridization with AuNp immobilized on the Au surface for the aflatoxin B1 sensor had a LOD of 1.04 pg/mL over a wide concentration range (0.0001 – 10 ng/mL).[39] This strategy has also been used by Hang and co-workers in detecting glucose by hybridizing AuNp with MIL-100(Fe), however, the resulting LOD is still relatively high (<12 mM).[26] Several studies have shown that AuNp could produce electromagnetic waves because there is a coupling effect of LSPR waves from AuNp with SPR propagation waves from the Au film.

In this report, the combination of these strategies has been employed to improve the performance of the UiO-66 modified SPR sensor chip as a glucose sensor. Investigation of the morphological effect was carried out using hierarchical plate-like (HPL) UiO-66 and UiO-66 synthesized by solvothermal method. The product was immobilized onto the Au layer of the standard SPR sensor chip by spin coating (SC) technique. The SPR measurements show that UiO-66 has higher performance with a LOD value of 0.784 mM (S/N = 3), which works in the concentration range of 0-10 mM. However, when compared with the direct assembly (DA) immobilization technique, the performance is lower. The LOD of UiO-66 with the DA technique is 0.389 mM in the same concentration range. The signal amplification effect was investigated by hybridizing UiO-66 and bipyramidal AuNp. The hybridization process is achieved by the solvothermal reaction of UiO-66 with AuNp bipyramid colloid obtained by the hydrothermal method. The synthesized products were immobilized onto a standard sensor chip by the DA technique. SPR measurements were carried out at lower concentrations first to determine the effect of signal amplification. The optimum glucose detection performance was obtained using the UiO-66 sample with the addition of AuNp bipyramid colloid (UiO-66/$Au_{0.5}$) which had a LOD value of ~3.4 times smaller than the pristine UiO-66 in the concentration range of 0.01-10 mM. In addition, selectivity of the UiO-66/$Au_{0.5}$ sample toward glucose was tested against related molecules, such as sucrose, uric acid, ascorbic acid, urea, and maltose. The results showed the excellent selectivity of UiO-66/$Au_{0.5}$ for glucose. Glucose detection tests were also carried out in human serum with

good recovery results, so the developed SPR sensor based on UiO-66/$Au_{0.5}$ has the potential to be used in practical glucose sensing applications.

2. Experimental section

2.1. Materials

Zirconium (IV) chloride ($ZrCl_4$, 99.5%), benzene-1,4- dicarboxylic acid (H_2BDC), gold (III) chloride hydrate ($HAuCl_4.xH_2O$, 99.995% trace metal basis), silver nitrate ($AgNO_3$, ≥99.0%), sodium borohydride ($NaBH_4$, 98%), cetyltrimethylammonium chloride solution (CTAC, 25%), acetic acid ($C_2H_4O_2$) solution, citric acid ($C_6H_8O_7$, 99%), hydrochloric acid (HCl, 1 M), sucrose (≥99.5% (GC)), uric acid ($C_5H_4N_4O_3$, ≥99%), 3-mercaptopropionic acid (3-MPA, ≥99%) and urea (CH_4N_2O) were purchased from Sigma-Aldrich (Japan and Singapore). *N, N*-dimethylformamide (DMF), and acetonitrile (C_2H_3N, 99.8%) and D(+)-glucose ($C_6H_{12}O_6$, 99.5%) were purchased from Fujifilm Wako Pure Chemical Corporation, Japan. Polyvinylpyrrolidone K-30 (PVP) (M_w = 40,000), maltose ($C_{12}H_{22}O_{11}$, ≥ 99%), and L-ascorbic acid ($C_6H_8O_6$, 99%) were purchased from Nacalai Tesque, Japan. Phosphate buffer saline (PBS) were purchased from Biogear Scientific (BioVentures, Inc., Iowa, USA). Commercial human serum (from male AB clotted whole blood) was purchased from Sigma-Aldrich, Singapore.

2.2. Synthesis of materials

Au seeds. The synthesis was carried out by the hydrothermal method with a water-based solution using a 50 mL vial. In an agitated state, 4 mL of 0.5 M CTAC was placed into a vial containing 32.1304 mL of distilled water, followed by the additions of 2 mL of 0.1 M citric acid solution, 0.87 mL of 0.01 M $HAuCl_4{\cdot}xH_2O$ solution, and 1.25 mL of 0.06238 M $NaBH_4$ solution. Afterward, the vial was closed and heated at 80 ºC for 90 min in an oil bath under magnetic stirring.

Bipyramidal AuNp. In a typical process, 40 mL of 0.1 M CTAC was placed into a 50 mL vial. Then, 2 mL of 0.01 M $HAuCl_4{\cdot}xH_2O$ solution, 0.4 mL of 0.01 M $AgNO_3$ solution, 0.8 mL of 1 M HCl solution, 0.32 mL of 0.1 M ascorbic acid solution, and 2 mL of Au seed, respectively were added into this solution. Then, the vial was closed and heated at 30 ºC for 2 h. Next, the mixture solution was centrifuged at 10,000 rpm for 20 min. Then, the water at the top was removed so that only the AuNp colloid remained in the centrifuge tubes. Finally, water was added again, and the centrifugation process was repeated until ~2 mL of colloidal AuNp was obtained.

Following this, AuNp colloid was prepared for the synthesis of UiO-66/AuNp. Typically, 12.8 mg of PVP was dissolved in 3 mL of DMF, then the AuNp colloid was added, and the solution was shaken for 24 h. Next, the resulting solution was washed with DMF and centrifuged for 10 minat 10,000 rpm. Then, the DMF in the AuNp colloid was discarded until ~2 mL of colloid was obtained. Then, DMF was added again until the colloid has a total volume of 5 mL.

UiO-66. The synthesis of UiO-66 and UiO-66/AuNp followed the procedures reported by Na *et al.* with some modifications.[43] In a typical procedure, 33.4 mg of $ZrCl_4$ was dissolved in 10 mL of DMF in a 20 mL vial and stirred until fully dissolved. After that, 25 mg of H_2BDC and 0.7 mL of acetic acid (36%) were added into this solution. Following this, the mixture solution was placed into the oven for 24 h at a temperature of 120 ºC. The resulting product was washed using DMF and methanol three times each and centrifuged at 14,000 rpm for 10 minutes. Finally, the product was dried in an oven at 60 ºC and then, in vacuum at 140 ºC overnight.

UiO-66/AuNp. The synthesis process for UiO-66/AuNp is almost similar as that for UiO-66, however, after the acetic acid addition, 0.0759 g of PVP was added and sonicated for 5 min. After that, 0.5 mL, 1 mL, and 2 mL of the above prepared AuNp colloid were added and the corresponding samples were labeled as UiO-66/$Au_{0.5}$, UiO-66/Au_1, and UiO-66/Au_2, respectively.

UiO-66 HPL. The UiO-66 HPL sample was synthesized according to our previous report.[44] Two different solutions were initially prepared, namely the metal precursor and the organic linker solutions. The metal precursor solution was prepared by dissolving 0.3 g of $ZrCl_4$ in 10 mL of DMF and 30 mL of acetonitrile, while the organic linker solution was made by dissolving 0.3 g of H_2BDC and 1.5 g of PVP in 30 mL of DMF and 10 mL of ACN. After that, 4 mL of each solution was taken and mixed in a 50 mL vial, then sonicated for 2 min. The vial was then heated in oil bath at 135 ºC for 24 h. The resulting product was washed by centrifugation at 14000 rpm for 8 min and dispersed in DMF, ethanol, and methanol three times in succession. After that, it was dried overnight in an oven at 60 ºC. Then, the dried UiO-66 powder was dispersed in chloroform and shaken for 24 h. Finally, the product was centrifuged and dried at 120 ºC overnight in a vacuum oven.

2.3. Materials characterization

The morphological characterization was performed using a scanning electron microscope (SEM, Hitachi SU-8000) operated at 10 kV and a transmission electron microscope (TEM, JEOL JEM2100F) operated at 200 kV. The ultraviolet-visible (UV-vis) spectra of the Au colloid (seed) and AuNp were collected using M-200 Pro Tecan, while the UV-vis spectra of UiO-66 and UiO-

66/AuNp were collected using JASCO V-570 UV-vis-NIR (NIR = near-infrared) spectrophotometer. The composition and crystal structure of the as-prepared samples were checked by X-ray diffraction (XRD, Rigaku RINT 2500X) with Cu-Kα radiation (λ= 0.15406 nm). Nitrogen (N_2) adsorption-desorption measurements were conducted using BELSOPR-max (BEL, Japan) at 77 K. The specific surface area and pore size distribution of each sample were calculated using the Brunauer-Emmett-Teller (BET) and nonlocal density functional theory (NLDFT) methods. Before the N_2 adsorption-desorption measurement, each sample was degassed at 175 ºC for 20 h. Raman spectra was collected with a 514.5 nm laser excitation on a HORIBA-JOBIN-YVON T64000 model. [COD 4512074, COD 1100138, and CCDC 733458 contains the supplementary crystallographic data used in this paper. These data can be obtained free of charge from the Crystallography Open Database (COD) via www.crystallography.net/cod and the Cambridge Crystallographic Data Center (CCDC) via www.ccdc.cam.ac.uk/data_request/cif.]

2.4. Sample immobilization onto standard SPR chip sensor

The sample suspension was made by dispersing 5 mg of each sample in 5 mL of methanol, followed by sonication in an ultrasonic bath for 30 min. Before immobilization by spin coating and direct assembly techniques, the 2 cm x 2 cm standard SPR sensor chip with a refractive index of 1.61 (composed of a glass substrate, 5 nm Cr layer, and 45 nm Au layer) (NanoSPR LLC, US) was cleaned by immersing it in piranha solution for 30 s followed by consecutive rinsing with tap water, soapy water, ethanol, and distilled water. After that, the SPR sensor chip was dried with an air blower. Next, 75 µL of 0.01 mM methanolic solution of MPA was dropped onto the surface of the sensor chip and left for 2 h. After that, the surface of the sensor chip was washed with methanol dried with an air blower.

The spin coating technique was carried out by dropping 200 µL of the prepared sample suspension onto the surface of the SPR sensor chip and then rotating it at 3000 rpm for 60 s and then drying at 100 ºC. The spin coating process was carried out three times. After that, the sensor chip was washed with PBS gently and dry using an air blower. The direct assembly technique was performed by dropping 100 µL of the sample suspension onto the surface of the SPR sensor chip followed by drying at room temperature for 12 h. Finally, the sensor chip was rinsed with PBS to remove the UiO-66 sample which is not tightly bound to the Au surface and dried using an air blower.

2.5. SPR measurements

SPR measurements were carried out using a NanoSPR 6 (NanoSPR LLC, US) device with a two-channel system. The dynamic response was measured in terms of the SPR intensity (*RU*) to time. Glucose solutions with wide concentration range from 0.1 to 10 mM were used to investigate the influence of morphology and immobilization techniques on the glucose sensing performance. The effect of signal amplification was studied using glucose concentration range of 0.01-10 mM. These glucose solutions were prepared by dissolving different amounts of D-glucose powder in PBS. The measurement process consisted of a baseline measurement using PBS for 15 minutes, a glucose association process for 20 minutes, and a dissociation process using PBS solution for 15 minutes. The flow rate used was 20 μL min^{-1} using a syringe pump.

2.6. Selectivity and reusability tests

The selectivity test was carried out by evaluating the response to glucose (0.1mM) against other compounds found in human blood. The competing biomolecules used were uric acid (UA), ascorbic acid (AA), urea (U), and maltose (M) with concentrations of 2.5 mM, 0.45 mM, 0.11 mM, 5 mM, and 0.1 mM, respectively. The concentration of these disruptive biomolecules was adjusted to the highest concentration limit in healthy human blood. Besides that, it was also tested on biomolecule with a similar structure to glucose, namely sucrose with a concentration of 2.5 mM. The reusability test was carried out on 2.5 mM glucose for five repetitions, sequentially without any other treatment, using a functionalized sample SPR chip with the best performance.

2.7. Glucose detection in human serum

The glucose solution in human serum was first prepared by dissolving the human serum in PBS with a volume ratio of 1:100 ($V_{\text{human serum}}$: V_{PBS}). This human serum solution was then used as solvent to prepare glucose solutions with concentrations of 0.01, 0.05, 0.1, 0.5, 1, 2.5, 5, and 10 mM. The measurement parameters for glucose SPR in blood serum were the same as those used in Section 2.5, except that the medium used for baseline measurement and the dissociation process is human serum solution.

3. Results and discussion

3.1. Synthesis and characterization

The morphology of the AuNp, UiO-66 and UiO-66/Au samples were characterized using both SEM and TEM, as shown in **Fig. 1**. The prepared AuNp have diverse morphologies including

bipyramidal, rod, and dumbbell-like morphology (**Fig. 1a**). In addition, there are also Au seeds that do not experience crystal growth. However, the majority of the AuNp exhibits bipyramid shape. This non-uniformity is caused by the low affinity of Cl^- from CTAC on Au in a solution containing Ag^+ so that the growth of the AuNp becomes more disordered.[45,46] In addition, the length of the heat-treatment time for seed formation greatly affects the formation of uniform AuNp. Specifically, the longer the heating time for Au seeds, the more uniform the shape of the resulting AuNp.[46]

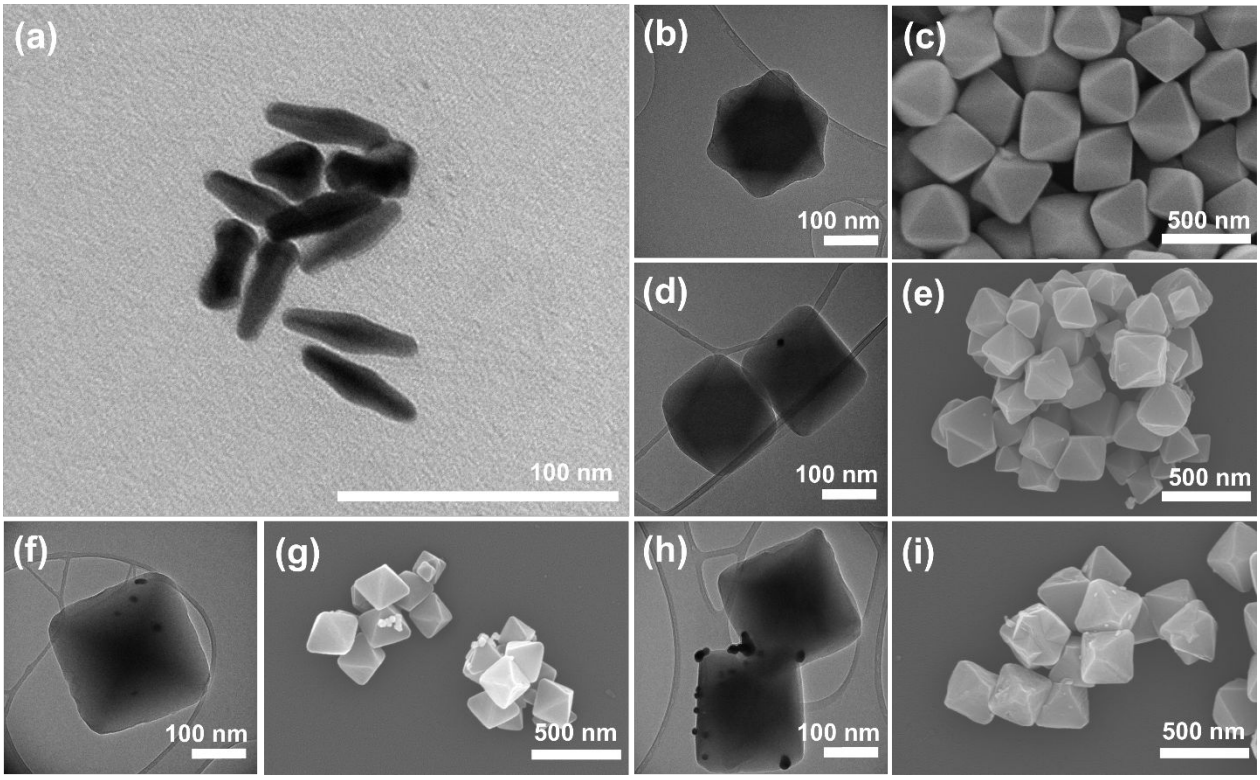

Fig. 1. TEM images of (a) AuNp, (b) UiO-66, (d)UiO-66/$Au_{0.5}$, (f)UiO-66/Au_1, and (h) UiO-66/Au_2, and SEM images of (c) UiO-66, (e)UiO-66/$Au_{0.5}$, (g)UiO-66/Au_1, and (i) UiO-66/Au_2.

The variation in the morphology of the synthesized AuNp can also be identified from the UV-vis spectra. In **Fig. S1a** (ESI), the UV-vis spectrum of AuNp shows two absorbance peaks at wavelengths (λ) of ~747 nm and ~529 nm. The appearance of these two peaks indicates that the morphology is not uniform. The peak at λ = ~529 nm is the Au seed spectrum, as shown in **Fig. S1a**, while the peak at λ = ~747 nm corresponds to bipyramidal AuNp. This is in agreement with

a previous report by Sánchez-Iglesias *et al.*, in which bipyramidal and rod AuNp exhibited peaks in the range of 730-1280 nm and these AuNp were synthesized using Au pentatwinned nanoparticles as seeds which showed a peak at 529 nm.[46] Therefore, the shape of the Au seed obtained from this study is similar to this work, namely pentatwinned nanoparticles. Furthermore, the absorbance peak at ~747 nm is higher than at ~520 nm, indicating that the amount of AuNp with bipyramidal shape is greater than the amount of AuNp with other shapes. The synthesized AuNp have peaks at ~38.08°, ~44.41°, and ~64.62°, which correspond to (110), (200), and (220) crystal planes of Au (Crystallography Open Database (COD) No. 1100138), respectively (**Fig. S1b**).[47]

The UiO-66 product synthesized using solvothermal method exhibit highly uniform octahedral morphology with an average size of ~250 nm (**Fig. 1c**). After adding colloidal AuNp to the UiO-66 precursor solution, the resulting UiO-66 particles become smaller in size and slightly less uniform. As depicted in **Fig. 1c, e, g, and i**, AuNp are attached to the surface of UiO-55/Au_1 and UiO-55/Au_2 but in the UiO-55/$Au_{0.5}$ sample, they are not visible. The TEM images in **Fig. 1b, d, f, and h** show the presence of AuNp in UiO-66. With increasing AuNp addition, more AuNp are deposited on the surface of UiO-66 particles. Additionally, the morphology of the AuNp also changes from bipyramid to spherical shape following the hybridization with UiO-66. This is because when the synthesis temperature starts to increase to 120 ºC, AuNp (Au^0) oxidation occurs with the help of Cl^- ions from $ZrCl_4$.[40] As a result, the AuNp become aggregated to reduce their surface energy and form larger spherical particles.[48,49] The agglomeration process may occur in the early stages of the hybridization process, and the possible growth mechanism is shown in **Fig. S2**. The SEM image of the HPL UiO-66 product reveals its hierarchical plate-like morphology (**Fig. S3a**) and the XRD pattern of HPL UiO-66 matches well with the simulated pattern of UiO-66, as seen in **Fig. S3b**.

The increase in LSPR activity due to the hybridization of UiO-66 with AuNp can be observed from the UV-vis spectra.[41] In **Fig. 2a**, increases in the absorbance of UiO-66 at certain wavelengths are observed. This increase varies depending on the volume of AuNp added, as seen in **Fig. 2b**. These peaks indicate the increased LSPR activity of UiO-66 after the hybridization with AuNp.[41,50] After AuNp are added to UiO-66, the LSPR peak is generally redshifted (**Fig. 2c**). UiO-66/$Au_{0.5}$,

UiO-66/Au_1, and UiO-66/Au_2 show LSPR activity at wavelengths of 538 nm, 536 nm, and 529 nm, respectively. However, after the addition of more than 0.5 mL of colloidal AuNp (UiO-66/$Au_{0.5}$ as the reference point), the wavelength experiences a blue shift. The redshift indicates an increase in the effective permittivity, while the blue shift indicates the opposite.[51] UiO-66/Au has an effective permittivity greater than UiO-66, then the effective permittivity of the hybrids follows the order of UiO-66/$Au_{0.5}$ > UiO-66/Au_1 > UiO-66/Au_2. Prior to hybridization, AuNp has a wavelength of 520 nm, and after hybridization with UiO-66, the AuNp LSPR peak in the UiO-66/Au sample changes to the values mentioned above (**Fig. S4a)**. This shift occurs due to the changes in the morphology of AuNp during the synthesis of UiO-66/Au. The hybridization process with UiO-66 seems to affect the shape of the AuNp. The LSPR peaks of all UiO-66/Au samples experience both broadening and red-shift, AuNp LSPR peak as a reference, **Fig. S4b**. These two phenomena indicate AuNp aggregation and an increase in the aspect ratio of AuNp.[52–54] The observed LSPR peak change in the UV-vis extinction spectra is due to shape change and agglomeration, thus changing characteristics of the free electron collective oscillation on the AuNp surface.[50,55,56] Therefore, the shape changes and agglomeration of AuNp observed in the TEM image are confirmed by the shift of the LSPR wavelength peak in the UV-vis spectra.

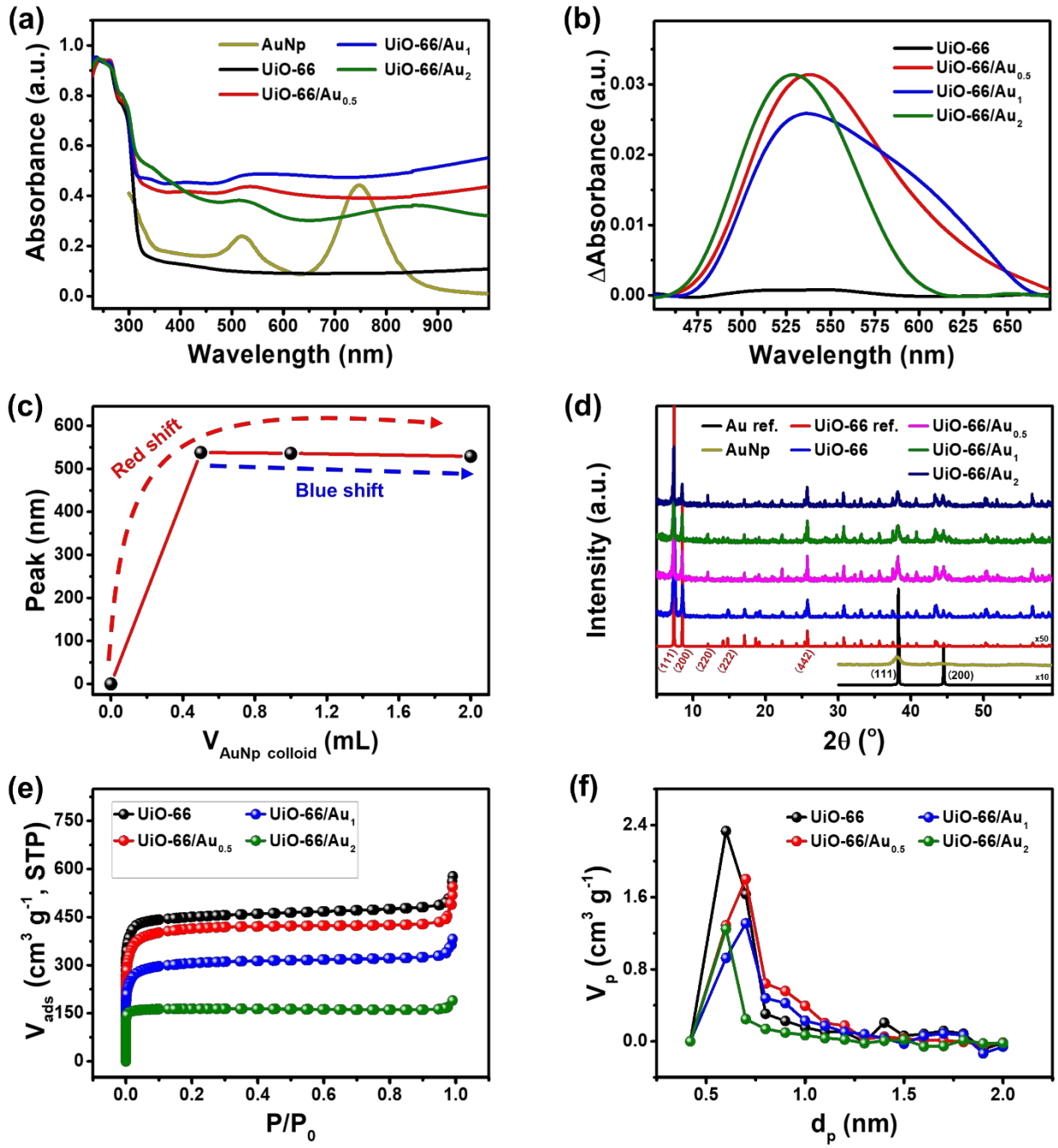

Fig. 2. (a) UV-vis spectra of AuNp, UiO-66, and UiO-66/Au. (b) Enlarged UV-vis spectra of UiO-66 and UiO-66/Au samples. (c) LSPR peak position as a function of the AuNp colloid volume addition to the UiO-66 precursor solution. (d) XRD patterns of UiO-66, UiO-66/$Au_{0.5}$, UiO-66/Au_1, and UiO-66/Au_2 and UiO-66 reference (COD. 4512074) and Au reference (COD. 1100138). (e) N_2 sorption isotherms and (f) NLDFT pore distribution plots of UiO-66 and UiO-66/Au samples.

For UiO-66/$Au_{0.5}$ and UiO-66/Au_1 samples, the LSPR wavelength peaks are not much different, but the LSPR intensity of the UiO-66/$Au_{0.5}$ sample is higher than that of UiO-66/Au_1. In

general, the greater the addition of AuNp colloid, the plasmonic properties of UiO-66 are improved. However, the larger the amount AuNp colloid added to the UiO-66 precursor solution, the greater the agglomeration possibility, as seen in UiO-66/Au_2, where bipyramidal Au aggregation occurs to form a new Au cluster, and its plasmonic activity and effective permittivity are lower than those of UiO-66/$Au_{0.5}$ and UiO-66/Au_1. The Au cluster in UiO-66/Au_2 exhibits a LSPR peak at ~855 nm, while the peaks in UiO-66/$Au_{0.5}$ and UiO-66/Au_1 are broad, so that they cannot be observed (**Fig. S5**).

The XRD patterns of the synthesized products are shown in **Fig. 2d**. The pristine UiO-66 sample has strong peaks at around 7.28°, 8.57°, and 25.74°, which correspond to (111), (200), and (442) planes of UiO-66 (COD No. 4512074), respectively, with *Fm-3m* space group and cubic crystal structure.[57] UiO-66/$Au_{0.5}$, UiO-66/Au_1, and UiO-66/Au_2 exhibit the same peaks as UiO-66, but some peaks are either increasing or decreasing in intensity. Specifically, the intensity of the (220) peak of UiO-66 at 12.01° increases, while the intensity of (222) peak of UiO-66 at 14.82° decreases. These changes may occur because of the use of PVP as a structure-directing agent in nanoparticle synthesis.[44,58] In comparison, HPL UiO-66 displays peaks at around 7.5°, 8.8°, and 17.5°, which correspond to (111), (200), and (400) planes of UiO-66 (Cambridge Crystallographic Data Center (CCDC) No. 733458), respectively, as reported by Cavka *et al*.[59]

The presence of AuNp in UiO-66/$Au_{0.5}$, UiO-66/Au_1, and UiO-66/Au_2 is indicated by the XRD peaks at ~38.24°, ~44.49°, and ~64.74°, which are indexed to the (111), (222), and (220) planes of Au. The changes in UiO-66 lattice parameters due to the addition of AuNp were obtained using the Rietveld refinement method in Profex 4.3.2a software. The strain (ϵ) on UiO-66 crystals as a result of the hybridization with AuNp is calculated using the Williamson-Hall equation as shown below:[60]

$$\beta\cos\theta = \frac{K\lambda}{D} + \epsilon 4\sin\theta \quad (1)$$

where D is the average crystallite size of UiO-66, K is the Scherrer constant, λ is the wavelength of XRD radiation (Cu-Kα = 0.15406 nm), β is the full width half maximum (FWHM) peak and intensity, and θ is the Bragg diffraction angle. The K value for cubic crystal structure of UiO-66 with (111) plane is 1.1547.[61] The ϵ value is obtained by plotting the graph with 4 sin θ as the x-axis and β cos θ as the y-axis. Then, by using linear regression, the slope value of the graph is the ϵ value. The obtained results from Rietveld refinement and calculation of the strain values are summarized in **Table S1**. From the table, the greater the amount of AuNp added, the greater the

lattice distance and the greater the strain on UiO-66 crystal, as shown in **Fig. 1h**. This is due to the increased decoration of AuNp on its surface.

The N_2 sorption measurements were carried out to determine the specific surface area (SSA) and pore distribution of the samples. The N_2 adsorption-desorption and the pore distribution plots of Au/UiO-66 and HPL UiO-66 samples are shown in **Fig. 2e-f** and **S3c-d**, respectively and the results are also summarized in **Table 1**. The pristine UiO-66 has the highest SSA among all the samples (1,784.0 $m^2 g^{-1}$) and this value is higher than the SSAs of other reported UiO-66 which varied in the range of 826.05-1,710 $m^2 g^{-1}$.[62–68] For UiO-66/Au samples, the hybridization with AuNp changes the SSA of UiO-66. The larger the AuNp colloid added, the smaller the SSA value. In addition, the total pore volume also decreases due to the partial pore blockage of UiO-66 by AuNp. The order of SSA from largest to smallest is UiO-66 > UiO-66/$Au_{0.5}$ > HPL UiO-66 > UiO-66/Au_1 > UiO-66/Au_2. The total pore volume of the samples follows the same trend as the SSA. The pore diameter calculated by the NLDFT method is not much different, which is in the range of 6-7 Å. The lack of significant change in the pore diameter of UiO-66 with increasing AuNp addition is likely because of these AuNp are only decorated on the surface of the UiO-66 particles and not inside them, thus pore blockage was not observed. A similar phenomenon is observed by Wang *et al.* where the average pore diameter of MOFs was only slightly changed from 0.6-0.7 nm to 0.64 nm after the addition of CuO nanoparticles.[69]

The pore diameter and total pore volume of HPL UiO-66 are much higher than other samples. The much larger pore diameter of UiO-66 HPL compared to UiO-66 is caused by the use of PVP as a structure modifier. In the crystal growth of HPL UiO-66, PVP coordinated with metal ions and occupied several sites in the organic linker around the Zr metal center through weak hydrogen bonds.[44,70,71] Then, the complex coordination process between PVP, organic linker, and the Zr metal center promotes hierarchical pores with larger pore diameters than pristine MOFs.[72] Further, Li *et al.* showed that the addition of PVP could enlarge the pore diameter by ~6.4 times larger compared to the pristine MOFs synthesized without PVP.[72]

Table 1. The BET specific surface area and pore size distribution of UiO-66, HPL UiO-66, UiO-66/$Au_{0.5}$, UiO-66/Au_1, and UiO-66/Au_2.

Sample	SSA ($m^2 g^{-1}$)	Pore diameter (Å)	Total pore volume ($cm^3 g^{-1}$)
UiO-66	1,784.0	6	0.7494
HPL UiO-66	1,248.4	26.6	1.9140
UiO-66/$Au_{0.5}$	1,597.8	7	0.6930
UiO-66/Au_1	1,177.3	7	0.5053
UiO-66/Au_2	668.13	6	0.2750

3.2. Detection of glucose

3.2.1. Effects of morphology and immobilization techniques

The morphological effects of UiO-66 were investigated using the octahedral and HPL form, named as UiO-66/SC and HPL UiO-66/SC, respectively, and each sample is immobilized onto the Au chip SPR sensor by the SC technique. The dynamic response of HPL UiO-66/SC and UiO-66/SC are shown in **Fig. 3**. Meanwhile, the change of intensity (ΔRU) values for each glucose concentration are shown in **Table S2**. At a concentration of 0.1 mM, the *RU* values of UiO-66/SC and HPL UiO-66/SC are not much different, but at concentrations between 0.5 and 10 mM, UiO-66/SC has higher *RU* values (**Fig. 3a** and **3c**). In addition, the signal characteristics of the two samples are also different which can be contributed by the different morphology.

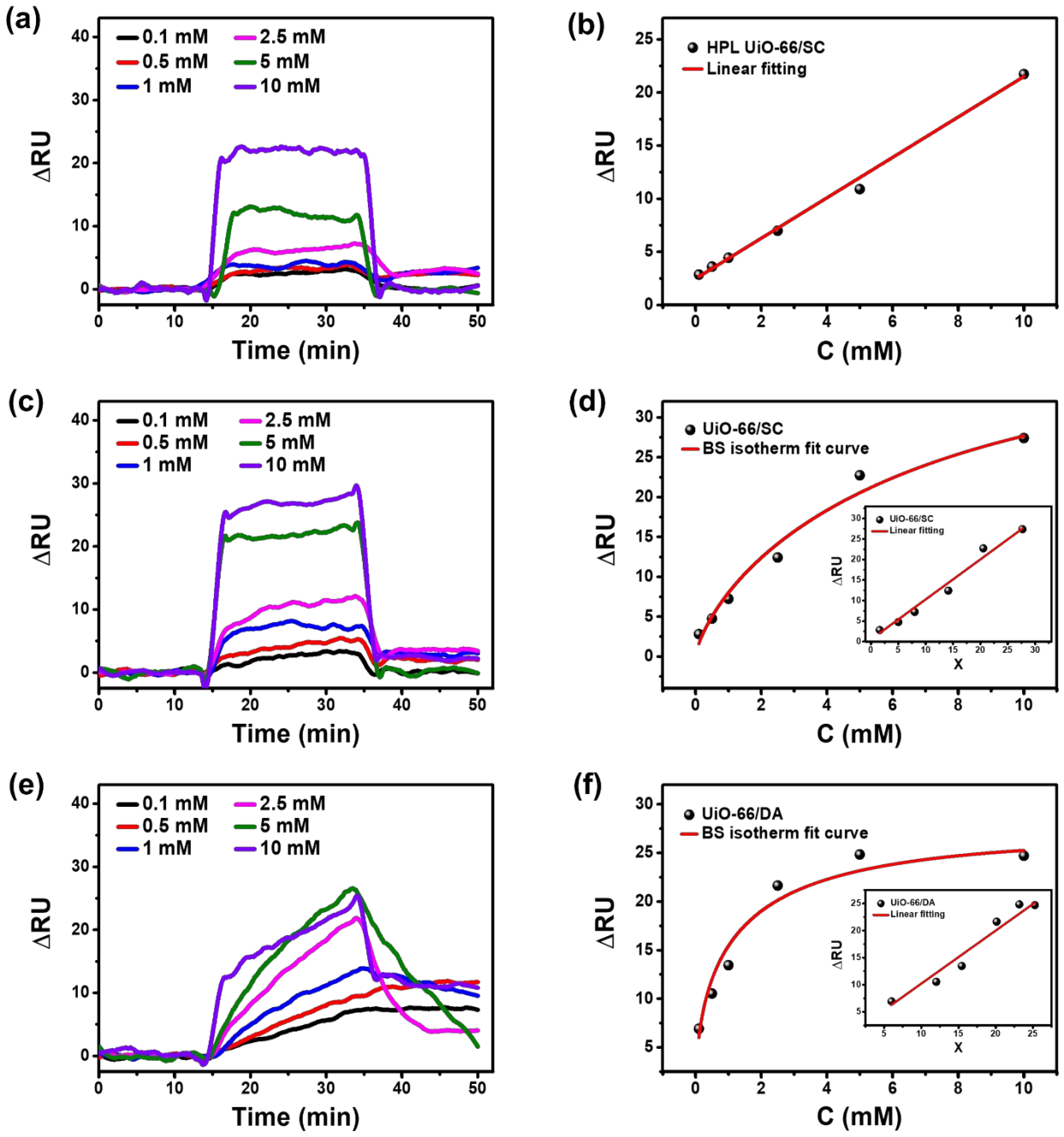

Fig. 3. The SPR sensor dynamic responses of (a) HPL UiO-66/SC, (c) UiO-66/SC, and (e) UiO-66/DA to glucose in the concentration range of 0.1-10 mM. Plots showing the changes in the dynamic response of the SPR sensor with increasing glucose concentration for (b) HPL UiO-66/SC, (d) UiO-66/SC, and (f) UiO-66/DA (the inset images show the corresponding calibration curves).

As shown in **Fig. 3b**, there is a linear correlation between the glucose concentration and the RU value for HPL UiO-66/SC in the concentration range of 0.1-10 mM with a correlation coefficient (R^2) of 0.9973 and a linear regression equation $\Delta RU = 1.9029X + 2.47464$, so that the LOD is 1.077 mM (S/N = 3), and the sensitivity value is 1.9029. For UiO-66/SC (**Fig. 3d**), the obtained experimental data corresponds to the Brouers-Sotolongo (BS) isotherm adsorption, which has the following equation (with slight modifications):[73]

$$\Delta RU = \Delta RU_m\left[1 - exp\left(-K_{BS}C^{\alpha}\right)\right] \quad (2)$$

where ΔRU is the unit change in reflectivity, ΔRU_m is the maximum adsorption capacity, K_{BS} is the BS constant, and α is the surface heterogeneity constant.[35,73] From the non-linear regression, the obtained R^2 value for UiO-66/SC is 0.9874 with the adsorption parameters $\Delta RU_m = 38.3109$, $K_{BS} = 0.2340$, and $\alpha = 0.7386$. To obtain the LOD and sensitivity, a linear form of **Eq. (2)** is used by plotting ΔRU *versus* $X = \Delta RU_m\,[1 - exp(-K_{BS}\,C^{\alpha})]$.[74] The linear equation obtained for UiO-66/SC is $\Delta RU = 0.9759X + 0.5259$ with $R^2 = 0.9884$. From this linear equation, the obtained LOD value is 0.784 mM (S/N = 3) with a sensitivity value of 0.9759.

Although the sensitivity of HPL UiO-66/SC is higher, UiO-66/SC shows better performance because it has a smaller LOD. The lower LOD of UiO-66/SC implies that this sensor has a better signal to noise ratio. The sensing performance is affected by both morphology and SSA. The SSA of UiO-66 is 1,748.0 $m^2\,g^{-1}$, while the SSA of HPL UiO-66 is 1,248.4 $m^2\,g^{-1}$. The higher SSA of UiO-66 relative to HPL UiO-66 allows for increased glucose adsorption. Moreover, the higher the glucose concentration, the greater the increase in the ΔRU value of UiO-66. Therefore, the hypothesis regarding the relationship between surface area, adsorption capacity and RU is well confirmed.

The sensing performance of UiO-66/SC was then compared with UiO-66 immobilized by the DA technique (UiO-66/DA). The dynamic response of UiO-66/DA is shown in **Fig. 3e**, and the calculation results are summarized in **Table S2**. The changes in ΔRU with glucose concentration for this sample also follows the BS isotherm model with R^2 value of 0.9739 (**Fig. 3f**). The ΔRU_m, K_{BS}, and α values of UiO-66/DA are 26.6981, 0.8629, and 0.5296, respectively. The calibration curve on the inset of **Fig. 3e** shows the linearity between ΔRU and $X = \Delta RU_m\,[1 - exp(-K_{BS}\,C^{\alpha})]$ with the linear equation $\Delta RU = 0.9804X + 0.3962$ with $R^2 = 0.9744$. From the linear regression, the LOD of UiO-66/DA is found to be 0.389 mM (S/N = 3) with a sensitivity value of 0.9804. Compared with UiO-66/SC, UiO-66/DA shows a lower LOD but higher sensitivity, so it can be

deduced that the use of DA technique can improve the glucose sensing performance of the SPR sensor.

This performance improvement can be analyzed using the obtained BS adsorption parameters. The α value of UiO-66/DA < UiO-66/SC < 1, suggesting that the glucose adsorption in UiO-66 follows the initial rapid biosorption kinetics. This is caused by the many active sites available on the surface that can absorb glucose molecules.[35] In other words, the smaller the α value, the more active sites available to absorb molecules. In addition, the smaller α value, the more homogeneous the surface characteristics are.[35] This factor plays a role in improving sensor performance. As the α value of UiO-66/DA is lower than that of UiO-66/SC, the active sites on the UiO-66 immobilized sensor with the DA technique are more numerous and homogeneous than the SC technique. Therefore, the immobilization technique used for the subsequent investigation will use the DA technique.

3.2.2. Signal amplification

To investigate the effect of signal amplification, all samples were immobilized by the DA technique. Hypothetically, the addition of AuNp to UiO-66 can increase the signal measurement by the SPR system. Therefore, the measurements were made using lower glucose concentrations than those used in Section 3.2.1. Specifically, the glucose concentrations used were 0.01, 0.05, 0.1, 0.5, 1, 2.5, 5, and 10 mM. The dynamic responses of the prepared SPR sensors with increasing glucose concentration are shown in **Fig. 4a-d**, with the *RU* values summarized in **Table S3**. Evidently, the changes in the *RU* value with increasing glucose concentration for UiO-66/$Au_{0.5}$, UiO-66/Au_1, and UiO-66/Au_2 are significantly different that those observed in UiO-66. The addition of AuNp to UiO-66 leads to significant changes especially at low glucose concentrations. In addition, upon exposure to 0.01 mM glucose, the signal generated by the pristine UiO-66 sample is difficult to be distinguished from the noise. However, this is not the case for the UiO-66/Au samples. Although the UiO-66/Au_1 sample exhibits a rather low RU value of 0.609 at a glucose concentration of 0.01 mM, the produced signal can still be distinguished from the noise.

The experimental data plots for all samples in **Fig. 4e** show that all curves follow the BS isotherm adsorption model with the R^2 values for UiO-66, UiO-66/$Au_{0.5}$, UiO-66/Au_1, and UiO-66/Au_2 being 0.9838, 0.9769, 0.9791, and 0.9769, respectively. The isotherm parameters from the non-linear regression analysis of the BS isotherm adsorption model on the experimental data are given in **Table 2**. Based on the α value, the characteristics of heterogeneity and the number of

active sites that interact with glucose on the sample surface are different. The α value follows the order of UiO-66 > UiO-66/Au_2 > UiO-66/Au_1 > UiO-66/$Au_{0.5}$, implying that the active sites in UiO-66/$Au_{0.5}$ are more numerous and homogeneous than those in the other samples. These parameters can affect the performance of the developed SPR sensor chip. For further investigations, the experimental data were calibrated using linear regression.

The linear regression curves for the BS isotherm adsorption model uses the linear form of **Eq. (2)** and they are shown in **Fig. 4f**. The linear regression analyses on the ΔRU vs. $X = \Delta RU_m [1 - exp(-K_{BS} C^{\alpha})]$ curves indicate the high R^2 values of 0.9822, 0.9781, 0.9771, and 0.9841 for UiO-66, UiO-66/$Au_{0.5}$, UiO-66/Au_1, and UiO-66/Au_2, respectively, with the linear equation and LOD calculation results (S/N = 3) shown in **Table 3**. The glucose sensing performance of the UiO-66 sensor chip, especially at low glucose concentrations, is increased due the signal enhancement effect by AuNp. The LOD values follow the order of UiO-66/$Au_{0.5}$ < UiO-66/Au_1 < UiO-66 < UiO-66/Au_2, indicating that the UiO-66/$Au_{0.5}$ immobilized sensor shows the highest performance. In addition, UiO-66/$Au_{0.5}$ also has a higher sensitivity than the other samples with the order of sensitivity being UiO-66/$Au_{0.5}$ > UiO-66/Au_1 > UiO-66/Au_2 > UiO-66. The above results indicate that the combined effect of the AuNp addition with SAA can improve the performance of non-enzymatic glucose sensors. The effect of AuNp on performance improvement will be studied more deeply in the adsorption and detection mechanisms section below.

Table 2. The obtained parameters from the non-linear regression of the BS adsorption model on the experimental data of UiO-66, UiO-66/$Au_{0.5}$, UiO-66/Au_1, and UiO-66/Au_2.

Sample	Parameters			
	R^2	α	K_{BS}	ΔRU_m
UiO-66	0.9838	0.6539	0.9305	25.7903
UiO-66/$Au_{0.5}$	0.9769	0.3397	0.9159	27.4923
UiO-66/Au_1	0.9791	0.5262	1.1061	15.7492
UiO-66/Au_2	0.9769	0.5670	0.5525	13.8546

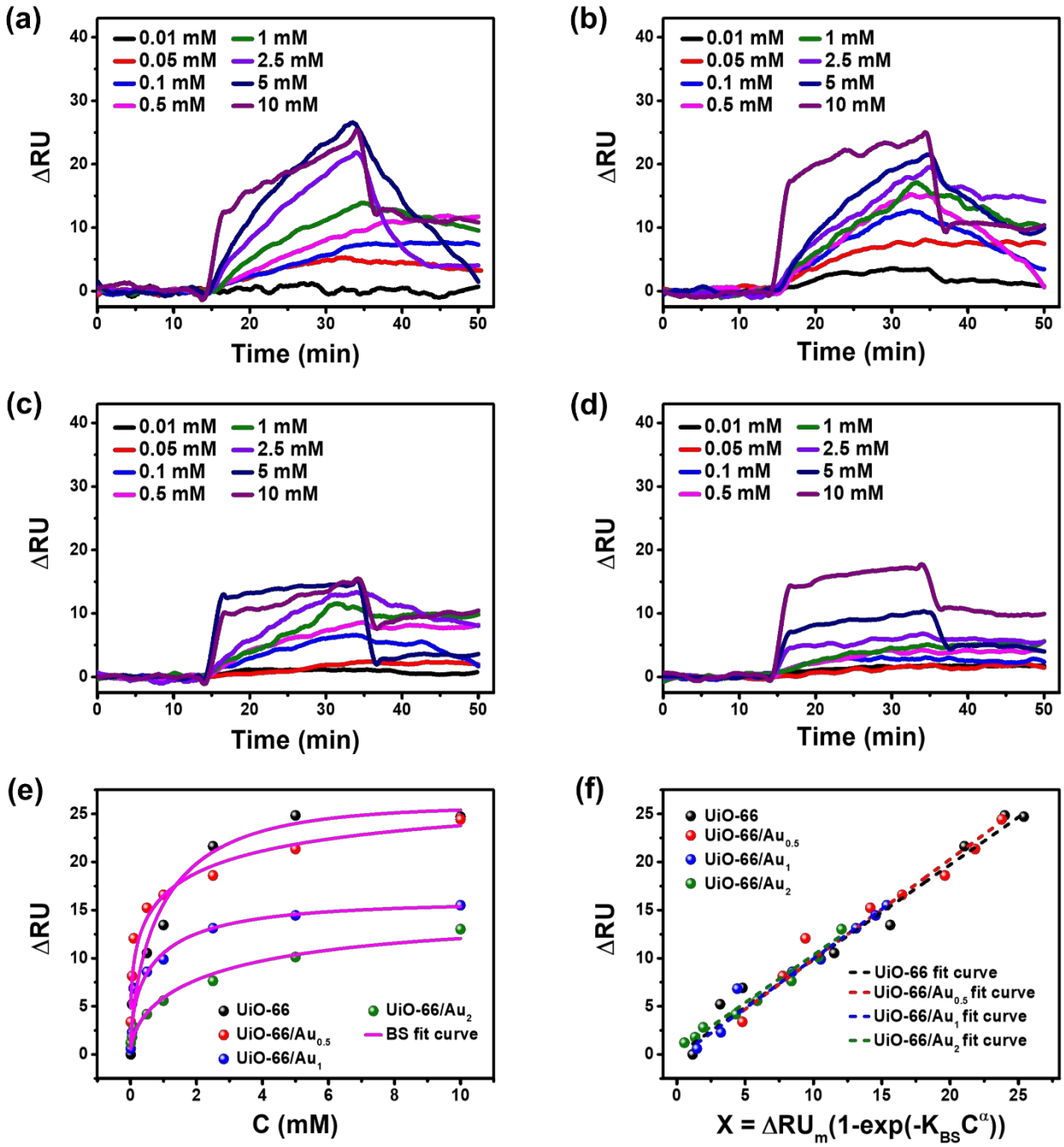

Fig. 4. The dynamic responses with increasing glucose concentration from 0.01 to 10 mM for (a) UiO-66, (b) UiO-66/$Au_{0.5}$, (c) UiO-66/Au_1, and (d) UiO-66/Au_2. (e) The concentration *versus* Δ*RU* curves and the non-linear regression analyses of the BS isotherm adsorption model and (f) the corresponding glucose detection calibration curves.

Table 3. The parameters obtained from calibration curves for UiO-66, UiO-66/$Au_{0.5}$, UiO-66/Au_1, and UiO-66/Au_2 for glucose detection in the concentration range of 0.01-10 mM.

Sample	Linear equation	R^2	Parameters LOD (mM) (S/N = 3)	Sensitivity
UiO-66	$\Delta RU = 0.9871X - 0.0248$	0.9822	0.2318	0.9871
UiO-66/$Au_{0.5}$	$\Delta RU = 1.0390X - 0.4922$	0.9781	0.0693	1.0390
UiO-66/Au_1	$\Delta RU = 1.0306X - 0.3529$	0.9771	0.1676	1.0306
UiO-66/Au_2	$\Delta RU = 0.9919X + 0.4176$	0.9841	0.2787	0.9919

A comparison of the glucose sensing performance of our MOF-based SPR sensors with previously developed SPR sensors is provided in **Table 4**. [4,7,11,26,75-79] Compared to other SPR sensors, the LOD value in this study is among the lowest, with a fairly wide concentration range, especially for the UiO-66/$Au_{0.5}$ sample. Almost all the obtained LODs in other studies are higher than 0.1 mM. Some fiber-based SPR sensors showed lower LOD values than UiO-66/$Au_{0.5}$ (0.055 mM and 0.01 mM).[7,75] However, in the study of Li *et al.*, the working range of the SPR sensor was too wide, and the process of mobilizing borate polymer onto the fiber/Au surface was quite complex. Further, Lobry *et al.* used Con A, which required potent adhesive compounds for the immobilization process onto the gold surface, thus complicating the fabrication process.

The use of MOFs as surface recognition has also been introduced in several reports.[11,26] In the report by Hang *et al.*, despite the use of AuNp to amplify the SPR signal, the LOD of this sensor is still lower than the LOD values of all samples in our study (**Table 4**). Furthermore, the working concentration range of a ZIF-8-based sensor with GO_x receptor was narrower (1-8 mM) than the optimum UiO-66/Au sensor. In our study, even without the use of bioreceptors, the UiO-66/$Au_{0.5}$ functionalized SPR sensor can operate in a wide concentration range of 0.01-10 mM with low LOD of 0.0693 mM (S/N = 3). As this sample can work in a relatively wide concentration range and has the lowest LOD among all the fabricated samples, it will be analyzed further in terms of its selectivity and reusability.

Table 4. The performance comparison of SPR-based glucose sensors with previous reports.

SPR type	Recognition surface	Concentration range	LOD	Ref.
Prism coupling	Au layer	0-140 mg/dl (0-7.77 mM)	6.23 mg/dL (0.3458 mM)	[76]
Prism coupling	CM5 chip with glucose/galactose-binding protein	1-30 mM	0.5 mM	[4]
Prism coupling	Au layer with polyindole/GO_x	0.075-0.5 μM	-	[77]
Optical fiber	Au layer with borate polymer	1-10 mg/dl (0.055-0.55 mM)	0.01 mg/mL (0.055 mM)	[75]
Prism coupling	Au layer with SiO_2/GO_x (glucose sensitive membrane)	0-80 mg/dl (0-4.44 mM)	4 mg/dL (0.22 mM)	[78]
LSPR	Au@MIL-100(Fe)	0-12 mM	< 12 mM	[26]
Tilt fiber bragg gratings (TFBGs)	Au layer with polydopamine/Con A	1-100 μM	0.01 μM	[7]
Long period grating (LPG)	ZIF-8/GO_x	1-8 mM	-	[11]
D-shaped optical fiber	Au layer with MoS_2-graphene/pyrene-1-boronic acid	0-300 mg/dl (0-16.65 mM)	-	[79]
Prism coupling	Au layer with HPL UiO-66	0.1-10 mM	1.077 mM	This work
Prism coupling	Au layer UiO-66 layer	0.01-10 mM	0.2318 mM	This work
Prism coupling	Au layer UiO-66/$Au_{0.5}$ layer	0.01-10 mM	0.0693 mM	This work

SPR type	Recognition surface	Concentration range	LOD	Ref.
Prism coupling	Au layer UiO-66/Au_1 layer	0.01-10 mM	0.1676 mM	This work
Prism coupling	Au layer UiO-66/Au_2 layer	0.01-10 mM	0.2787 mM	This work

3.2.3. Raman spectroscopy and possible sensing mechanism

The Raman spectra taken from 200 to 1800 cm^{-1} show increases in the peak intensity of the samples before and after glucose exposure (**Fig. 5a, b**). Both UiO-66 and UiO-66/$Au_{0.5}$ experience several increases in peak intensity after exposure to glucose. The peak strengthening at 630 and 860 cm^{-1} are attributed to the ν(C−C) aliphatic chain vibration and the linker C−H in-plane bending mode. The peak at 1140 cm^{-1} indicates a breathing mode in the terephthalate ring. The strengthened peaks at 1428 and 1450 cm^{-1} correspond to the in-phase carboxylate stretching normal mode. Furthermore, the peak increase at 1613 cm^{-1} can be indexed to the C−C bond stretching mode of the linker aromatic ring.[80] Several other peaks also experience slight enhancements, indicating the appearance of functional groups belonging to glucose. The peaks at 200-500 cm^{-1} represent the main skeletal vibrational motions of glucose which correspond to δ(C−C−C), δ(C−C−O), and τ(C−C). In addition, the peak strengthening between 820-950 cm^{-1} can be assigned to the vibrational ν(C−O), δ(C−C−H), ν(C−C), and δ(C−C−O) specifically induced by glucose.[81] In line with Bock et al. work, the presence of glucose is indicated by the Raman peaks at 542, 843, 916, and 1272 cm^{-1}.[82] The intensity peak at 1125 cm^{-1} is also a glucose-specific peak corresponding to the asymmetric ν(C−O−C).[83] Therefore, it is clear that UiO-66 and UiO-66/Au0.5 can bind glucose well.

Zeng *et al.* showed that the glucose adsorption process by UiO-66 involves the interaction of the hydroxyl functional group (O−H) in UiO-66 with that in glucose through hydrogen bonding.[23] The hydrogen bonding involves van der Waals forces and is influenced by the attractive dipole-dipole interactions.[84] In this work, the dipoles are the O−H groups of glucose and UiO-66. Therefore, when glucose meets the surface of UiO-66 and UiO-66/Au, the O−H group of glucose was bound to the hydroxyl terminal and bridge of UiO-66 with an initial rapid kinetic biosorption mechanism. If viewed from the dynamic responses of UiO-66 and UiO-66/Au (**Fig. 4**), the response

curves during the dissociation process are observed to either return to the initial baseline or above the baseline. This phenomenon indicates that the O−H groups on UiO-66 and UiO-66/Au are bound strongly to the O−H group of glucose. However, no dissociation curve is observed with a lower response value than the baseline value. Therefore, during the association and dissociation processes, there is no release of UiO-66 or UiO-66/Au from the surface of the SPR sensor chip, and the shedding phenomenon does not occur.

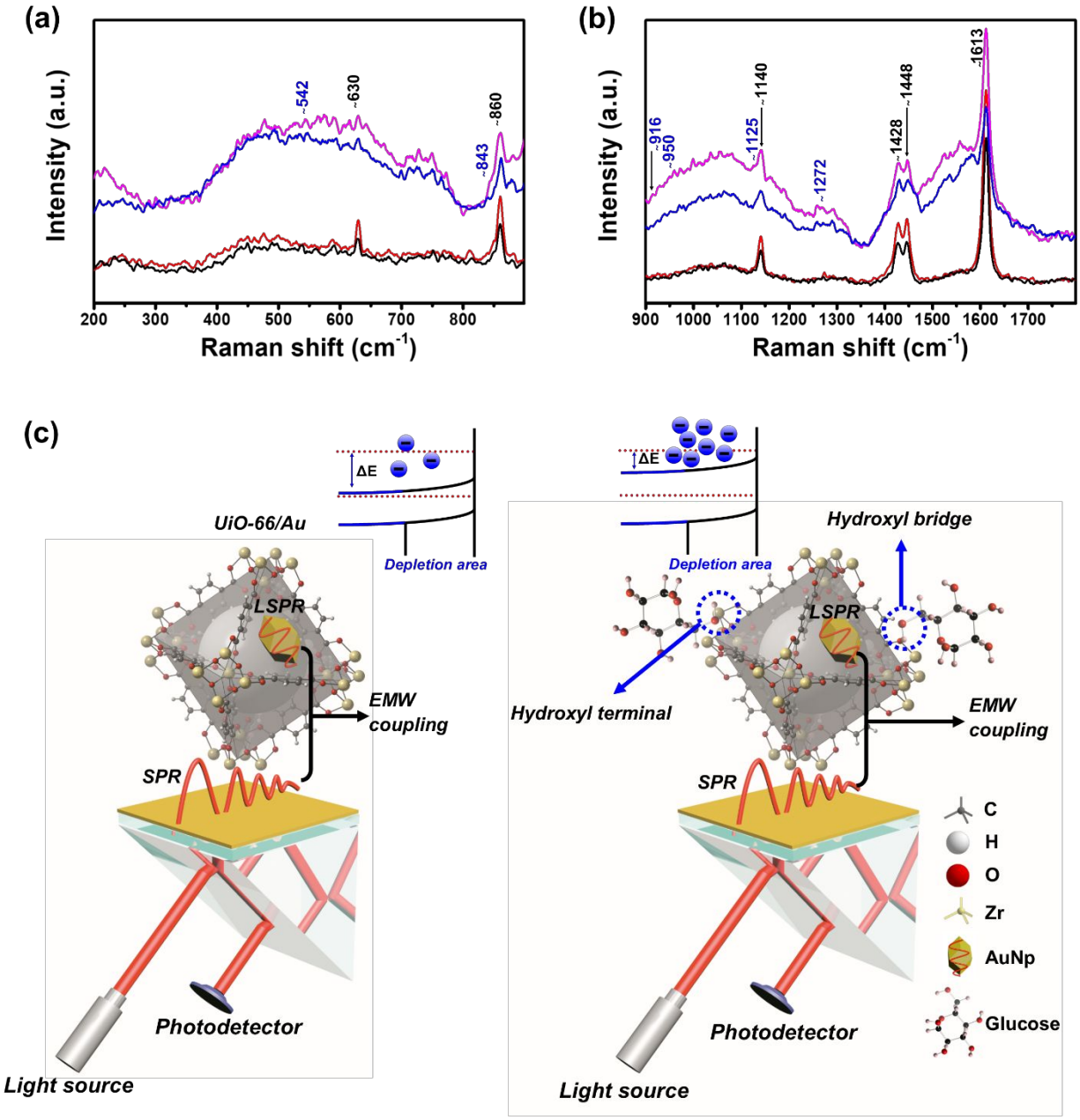

Fig. 5. Raman spectra of UiO-66 [before (black line) and after (red line) glucose exposure] and UiO-66/$Au_{0.5}$ [before (blue line) and after (magenta line) glucose exposure] in the range of (a) 200-

900 cm^{-1} and (b) 900-1800 cm^{-1}. (c) The possible mechanism of glucose sensing by UiO-66/Au.

The detection mechanism of the SPR is strongly influenced by the refractive index and the medium dielectric constant above the Au layer surface of the SPR chip. When the laser strikes the Au layer, the free electrons interact with the photon energy to experience brief exponential oscillations and propagate (electromagnetic evanescence wave) at the Au-dielectric interface. AuNp in UiO-66 exerts an amplification effect on the signal through the coupling mechanism of the AuNp LSPR wave with electromagnetic waves generated by the Au surface on the SPR sensor chip.[37–39] The proposed glucose detection mechanism is shown in **Fig. 5c**. The coupling between SPR and LSPR waves can be viewed through the depth of penetration of electromagnetic waves (EMW) generated by the SPR sensor chip by using the wave vector equation in the direction of the normal plane. The equations are expressed as below:[85]

$$k_{zi} = \frac{2\pi}{\lambda}\sqrt{\frac{{\varepsilon_i}^2}{\varepsilon_1 + \varepsilon_2}} \quad (4)$$

$$z_i = \frac{1}{k_{zi}} \quad (5)$$

where λ is the wavelength (λ (NanoSPR6) = 650 nm), ε_1 and ε_2 are the metal dielectric permittivity and the medium dielectric permittivity, respectively. k_{zi} is the wave vector in the normal plane direction, and z_i is the penetration depth. The refractive index (n) value of the NanoSPR 6 sensor chip is 1.61, and the n value of PBS is 1.3348.[86] Through the relationship $n = \sqrt{\varepsilon}$, the ε_{chip} is 2.5921, and ε_{PBS} is 1.7817. Furthermore, by using **Eqs. (4) and (5)**, the penetration depth of EMW is determined to be 121.383 nm. If it is assumed that AuNp is precisely in the middle of UiO-66, then the EMW can directly affect AuNp because UiO-66 has an average size of ~125 nm and AuNp has an average size of ~76,352 nm. If the size of the AuNp is smaller than the EMW penetration depth of the SPR layer, an increase in SPR signal may occur.[87]

Before the glucose solutions were exposed to UiO-66/Au, a laser fired at the surface of the Au chip resulted in the excitation of SPR waves in the form of EMW oscillations on the surface and propagated perpendicularly. Simultaneously, the AuNp at UiO-66/Au produce LSPR waves in the form of electron oscillations around the AuNp surface.[88] This results in an increase in EMW generated through the coupling mechanism of SPR and LSPR waves.[38,39,88] When the UiO-66/Au active sites bind glucose, the interacting dipole-dipole (*i.e.*, $O{-}H_{UiO\text{-}66/Au} - O{-}H_{glucose}$) becomes polarized under the influence of the EM field generated by the coupling of the SPR and LSPR

waves. In this state, the Fermi energy shifts and causes a change in the interface permittivity.[89,90] Other optical constants, such as the interface dielectric constant and the interface refractive index, also change.[89] Changes in these constants subsequently affect the SPR reflection angle and laser intensities that are read by the photodetector. The EMW on UiO-66 without the AuNp addition is only sourced from the evanescence waves of the sensor chip Au layer, so the resulting performance is not better than the UiO-66/Au samples.

UiO-66/$Au_{0.5}$ has the smallest α value and the largest ΔRU_m, so it is not surprising that it has the highest performance because its surface is the most homogeneous and provides the largest adsorption capacity with the largest number of active sites. Hence, although its plasmonic properties are not greater than UiO-66/Au_1, these two parameters have significant impact. The higher α value of UiO-66/Au_1 than UiO-66/$Au_{0.5}$ indicates its heterogeneous surface with fewer active sites, thus leading to its lower adsorption capacity and sensing performance compared to UiO-66/$Au_{0.5}$. These observations suggest that the signal enhancement by the coupling of LSPR and SPR wave is less effective in improving sensor performance if it is not accompanied by the ability to bind as much glucose as possible. Similarly, although UiO-66/Au_2 has better plasmonic properties than UiO-66, its adsorption capacity is lower due to the greater amount of agglomerated AuNp which may block or cover its active sites.

3.3. Selectivity and reusability

As seen in **Fig. 6a** and **b**, the selectivity test results show that UiO-66/$Au_{0.5}$ has the highest response to 0.1 mM glucose than other competing compounds, even though the concentration is far below the minimum blood glucose limit. In contrast, the concentration of other compounds is the maximum concentration in healthy people. The *RU* and the selectivity coefficient (*k*) can be seen in **Table 5**. The *k* value is obtained using the following equation:[91]

$$k = \frac{\Delta RU_{template}}{\Delta RU_{competitor}} \quad (6)$$

where *k* is the selectivity coefficient, $\Delta RU_{template}$ is the *RU* change due to the main biomolecule (glucose), and $\Delta RU_{competitor}$ is the RU change from the dynamic response of competing biomolecules. The *k* value reflects the selectivity of UiO-66/$Au_{0.5}$ to glucose against other competing compounds. If $k > 1$, then the selectivity is higher toward glucose and if $k < 1$, then it is more selective against competing compounds.

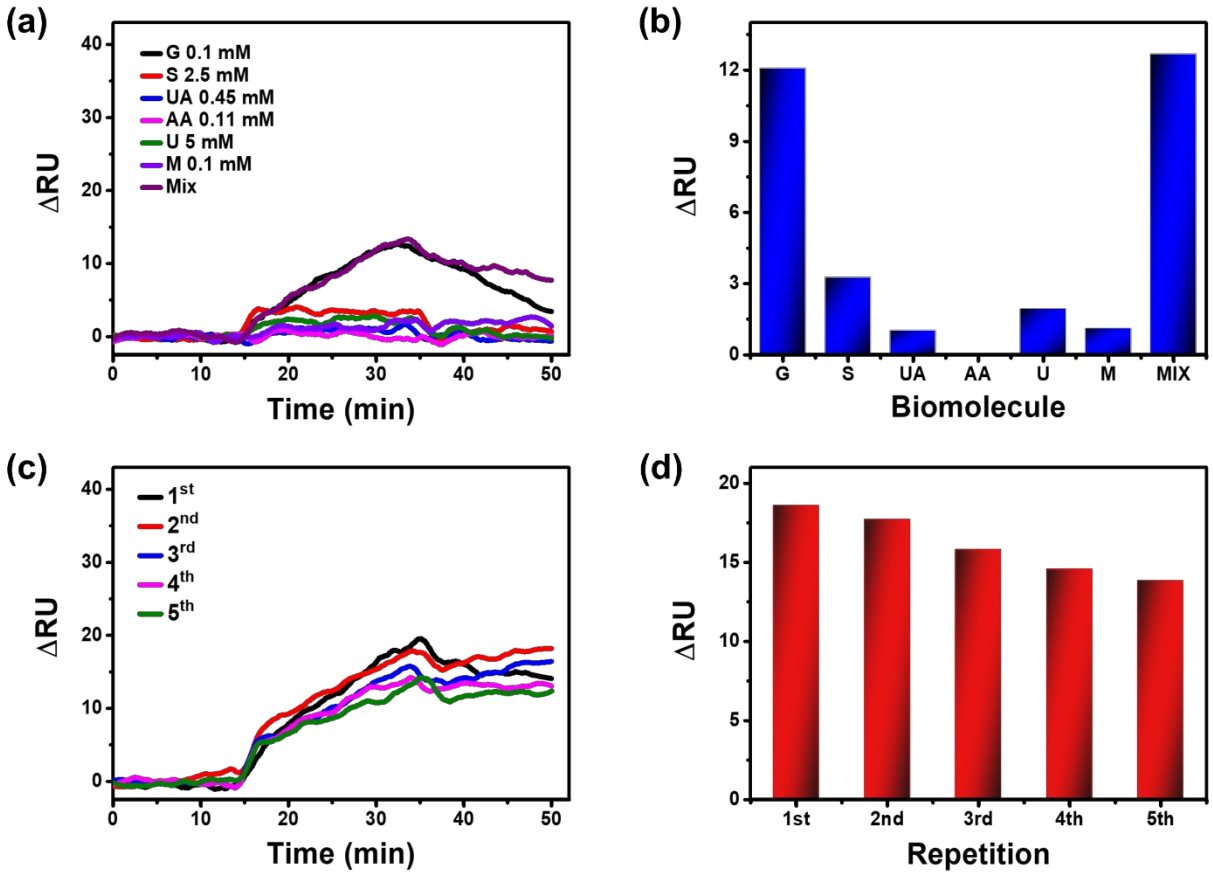

Fig. 6. Selectivity test results: (a) Dynamic responses of UiO-66/Au0.5 SPR sensor to 0.1 mM glucose and other competing compounds (2.5 mM S, 0.45 mM UA, 0.11 mM AA, 5 mM U, and 0.1 mM M) and their mixtures (MIX, without S), and (b) a bar chart comparing the responses of UiO-66/$Au_{0.5}$ to glucose and other compounds as obtained from the dynamic response data. Reusability test results: (c) Dynamic responses of UiO-66/$Au_{0.5}$ SPR sensor to 2.5 mM glucose from the first to fifth measurement and (d) the corresponding plot showing the changes in response with repetition number.

The *RU* of competing compounds from largest to smallest is G > S > U > M > UA > AA with selectivity coefficients of *k* (S) = 3.2499, *k* (U) = 6.2661, *k* (M) = 10.9377, *k* (UA) = 11.9192, and *k* (AA) = 442.2344. All competing compounds have *k* values > 1, indicating that UiO-66/$Au_{0.5}$ is not more selective to them. To ensure that the glucose response signal can be distinguished from these competing compounds, an additional selectivity test was carried out using a mixture of all biomolecules (except for S), with the same concentration as before. The *RU* value of MIX (a mixture of G, UA, AA, U, and M) is 12.680 and the *k* value of 0.9522. The *RU* of MIX

biomolecules is not much different from the Δ*RU* value for 0.1 mM glucose, and the *k* value is close to 1. Therefore, it can be concluded that UiO-66/$Au_{0.5}$ is more likely to interact with glucose than other competing compounds.

Table 5. The Δ*RU* values and selectivity coefficients of UiO-66/$Au_{0.5}$ toward glucose and competing biomolecules.

Biomolecule	**Δ*RU***	***k***	**Biomolecule**	**Δ*RU***	***k***
G	12.073	-	U	1.9267	6.2661
S	3.2499	3.7149	M	1.1038	10.938
UA	1.0129	11.919	MIX	12.680	0.9522
AA	0.0273	442.23			

The reusability test of UiO-66/$Au_{0.5}$ for glucose detection is shown in **Fig. 6c**. It can be observed that there is a gradual decrease in the Δ*RU* value with increased repetition/cycling. Compared with the first measurement, the second until fifth measurement percentages are 95.16%, 84.97 %, 78.34%, and 74.44% (**Fig. 6d**). The relatively strong binding of glucose to UiO-66/$Au_{0.5}$ can cause this decrease and the dissociation process using PBS does not entirely release the bound glucose molecules. The dynamic response data in **Fig. 6c** supports this explanation because when the dissociation process is carried out, the signal does not return to the baseline position before the exposure to glucose.

The inability of the response to return to the baseline during the dissociation process indicates that the sensor chip regeneration is not very good. There are several factors that can cause this problem, including a combination of chemical compounds, concentration, and regeneration contact time with the regeneration rate (k_{off}) dissociation having the order of 10^{-4} s^{-1}.[92] In this study, to determine whether the desorption rate is detrimental to the regeneration process, an analysis using a kinetic adsorption model was carried out through a non-linear fitting on the experimental data of 2.5 mM glucose dissociation. The regeneration curve (**Fig. S6**) seems to correspond to Avrami's kinetic adsorption model represented by the equation:[73,74]

$$\Delta RU_t = \Delta RU_e \left\{1 - \exp\left[-(k_{AV}t)\right]^{n_{AV}}\right\} \qquad (7)$$

where ΔRU_t is the change in intensity over time, k_{AV} is the kinetic constant or adsorption/desorption rate, and n_{AV} is the Avrami constant. The value of R^2 obtained from the non-linear regression analysis is 0.9786 with k_{AV} of 0.038624 s^{-1} and $n_{AV} = -0.2422$. The k_{AV} is much greater than the

minimum requirement for a perfect regeneration process. Hence, it can be concluded that the rate of desorption is not detrimental for the regeneration process. Therefore, the factors that may reduce the regeneration are the combination of chemical compounds and the concentration of the medium used.

3.4. Glucose detection in human serum

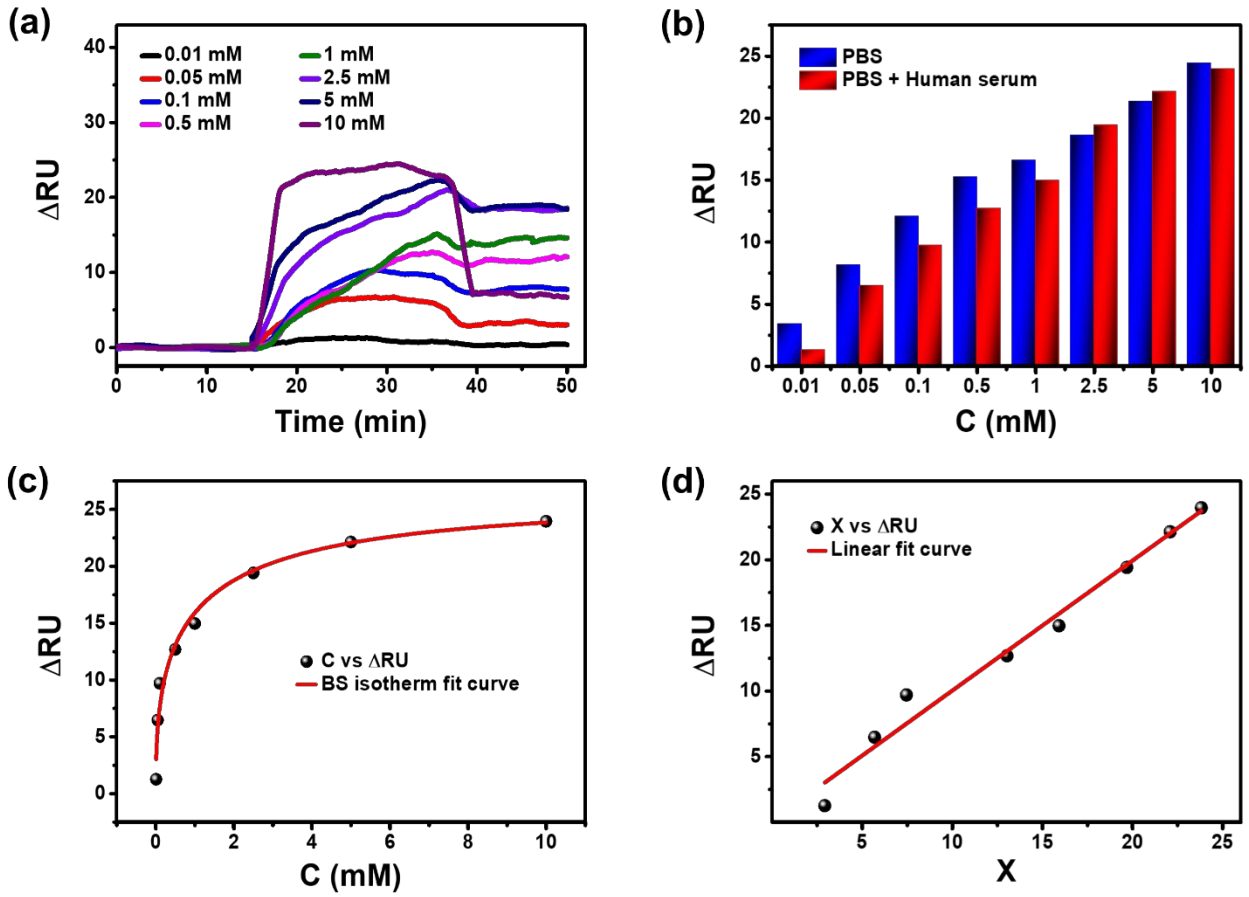

Fig. 7. (a) The dynamic response of UiO-66/$Au_{0.5}$-based SPR sensor to 0.1-10 mM glucose in a mixture of human serum and PBS solution. (b) A bar chart comparing the *RU* values measured for each glucose concentration in PBS solution and human serum/PBS mixture solution. (c) The concentration *versus* Δ*RU* curve and its non-linear regression analysis of the BS isotherm adsorption model. (d) The calibration curve for glucose detection in human serum/PBS mixture solution.

To assess the suitability of the SPR sensor based on UiO-66/$Au_{0.5}$ for practical applications, the measurements were performed on a glucose solution in a mixture of PBS and commercial human serum (volume ratio of 100:1) with similar concentrations as before. The dynamic response results shown in **Fig. 7a** reveal that the response increases with increasing glucose concentration. Then, when compared with the change in the dynamic response of the test without human serum (**Fig. 7b**), the magnitude is not much different. This difference appears to be due to the use of human serum. From **Table S4**, it can be seen that the UiO-66/$Au_{0.5}$ sensor displays variable recovery values depending on the glucose concentration. The recovery values at glucose concentrations of 0.01 mM, 0.05 mM, 0.1 mM, 0.5 mM, 1 mM, 2.5 mM, 5 mM, and 10 mM are 37.51%, 79.49%, 80.36%, 83.24 %, 90.26 %, 104.37 %, 103.69 %, and 98.08%, respectively. However, to determine the recovery values that represent all glucose concentrations, it is necessary to calibrate the response data. The concentration *versus* ΔRU curve (**Fig. 7c**) follows the BS isotherm adsorption model with an R^2 value of 0.9819. Next, using its linear form, we get the linear equation $\Delta RU = 0.9904X + 0.13391$ with $R^2 = 0.9782$, as seen in **Fig. 7d**. The slope value of this linear equation corresponds to the sensitivity value which is 0.9904. Then, comparing this slope value with the linear equation slope of the UiO-66/$Au_{0.5}$ sensor chip without using human serum, the overall recovery value is determined to be 95.33%. This high recovery value suggests that the developed sensor could work in practical applications and has great potential as a sensor to control diabetes.

4. Conclusions

In summary, this study describes the performance enhancement of the UiO-66 functionalized SPR sensor in glucose detection by optimizing its morphology, immobilization technique and adding AuNp to amplify the signal during glucose detection. Based on the results obtained, the morphology can affect its performance. With the same immobilization technique, the octahedral UiO-66 has a smaller LOD than the HPL UiO-66 in the working range of 0.1 to 10 mM, which is attributed to its much larger SSA. In addition, the most effective immobilization technique for improving performance is the DA technique. The LOD of UiO-66 immobilized by this technique is lower than that immobilized by the SC technique in the glucose concentration range of 0.1-10 mM. This is due to the more homogeneous surface layer (indicated by the value of $\alpha < 1$), so it has a higher amount of active sites for glucose binding. Furthermore, the modification of UiO-66 with AuNp can also improve the performance of the glucose SPR sensor. By using the DA immobilization technique, the LOD value follows the order of UiO-66/$Au_{0.5}$ < UiO-66/Au_1 < UiO-

66 < UiO-66/Au_2. This indicates the superior glucose sensing performance of UiO-66/$Au_{0.5}$ with a LOD of 0.0693 mM (S/N = 3) in the concentration range of 0.01-10 mM. The combined high SSA and LSPR effect of UiO-66/$Au_{0.5}$ directly enhance the glucose adsorption capacity and lower the LOD, thus improving the SPR performance for glucose detection. This study is expected to provide a new perspective in exploiting the unique properties of UiO-66 and its hybrids for glucose sensing applications using SPR technology. Apart from being an active material to increase glucose adsorption capacity, UiO-66/$Au_{0.5}$ also has a good and acceptable recoveries value, indicating its promising potential for practical glucose sensing applications.

Conflicts of Interest

There are no conflicts to declare

Acknowledgements

The authors acknowledge financial grants provided by Lembaga Pengelola Dana Pendidikan (LPDP), Ministry of Finance of Indonesia. This work is also partially supported by Indonesia Ministry of Education and Culture, and Indonesia Ministry of Research and Technology under grant scheme of World Class University Program managed by Institut Teknologi Bandung. J. H. acknowledge the funding from Japan Society for the Promotion of Science (JSPS) KAKENHI Program (Grant No. 20K05453). Y. Y acknowledges the financial support from the JST-ERATO Yamauchi Materials Space-Tectonics Project (JPMJER2003). Y. V. K. acknowledges the funding from Advance Queensland (AQIRF043-2020-CV). M. A. A. is grateful to the Taif University Researchers Supporting Project number (TURSP-2020/03), Taif University, Taif, KSA. This work was performed in part at the Queensland node of the Australian National Fabrication Facility (ANFF), a company established under the National Collaborative Research Infrastructure Strategy to provide nano and microfabrication facilities for Australia's researchers.

References

1 R. B. M. Schasfoort and A. J. Tudos, *Handbook of Surface Plasmon Resonance: Edition 2*, Royal Chemistry society, Cambridge, 2nd edn., 2017.

2 S. Li, Q. Wu, P. Ma, Y. Zhang, D. Song, X. Wang and Y. Sun, *Talanta*, 2018, **180**, 156–161.

3 J. Li, D. Lu, Z. Zhang, Q. Liu and Z. Qi, *Sens. Actuators B*, 2014, **203**, 690–696.

4 H. V Hsieh, Z. A. Pfeiffer, T. J. Amiss, D. B. Sherman and J. B. Pitner, *Biosens. Bioelectron.*, 2004, **19**, 653–660.

5 H.-C. Wang and A.-R. Lee, *J. Food Drug Anal.*, 2015, **23**, 191–200.

6 M.-S. Steiner, A. Duerkop and O. S. Wolfbeis, *Chem. Soc. Rev.*, 2011, **40**, 4805–4839.

7 M. Lobry, D. Lahem, M. Loyez, M. Debliquy, K. Chah, M. David and C. Caucheteur, *Biosens. Bioelectron.*, 2019, **142**, 111506.

8 A. Stephenson-Brown, H.-C. Wang, P. Iqbal, J. A. Preece, Y. Long, J. S. Fossey, T. D. James and P. M. Mendes, *Analyst*, 2013, **138**, 7140–7145.

9 R. Ballerstadt, C. Evans, R. McNichols and A. Gowda, *Biosens. Bioelectron.*, 2006, **22**, 275–284.

10 N. K. Singh, B. Jain and S. Annapoorni, *Sens. Actuators B*, 2011, **156**, 383–387.

11 G. Zhu, M. Zhang, L. Lu, X. Lou, M. Dong and L. Zhu, *Sens. Actuators B*, 2019, **288**, 12–19.

12 L. E. Kreno, J. T. Hupp and R. P. Van Duyne, *Anal. Chem.*, 2010, **82**, 8042–8046.

13 X. Jiang, S. He, G. Han, J. Long, S. Li, C. H. Lau, S. Zhang and L. Shao, *ACS Appl. Mater. Interfaces*, 2021, **13**, 11296–11305.

14 Y. Zhang, X. Cheng, X. Jiang, J. J. Urban, C. H. Lau, S. Liu and L. Shao, *Mater. Today*, 2020, **36**, 40–47.

15 J. Pei, K. Shao, J.-X. Wang, H.-M. Wen, Y. Yang, Y. Cui, R. Krishna, B. Li and G. Qian, *Adv. Mater.*, 2020, **32**, 1908275.

16 Y.-F. Zhang, Z.-H. Zhang, L. Ritter, H. Fang, Q. Wang, B. Space, Y.-B. Zhang, D.-X. Xue and J. Bai, *J. Am. Chem. Soc.*, 2021, **143**, 12202–12211.

17 I. Hussain, S. Iqbal, T. Hussain, Y. Chen, M. Ahmad, M. S. Javed, A. AlFantazi and K. Zhang, *J. Mater. Chem. A*, 2021, **9**, 17790–17800.

18 R. K. Tripathy, A. K. Samantara and J. N. Behera, *Sustain. Energy Fuels*, 2021, **5**, 1184–

1193.

19 D. Ma, Y. Zhang, S. Jiao, J. Li, K. Liu and Z. Shi, *Chem. Commun.*, 2019, **55**, 14347–14350.

20 S. Babaee, M. Zarei and M. A. Zolfigol, *RSC Adv.*, 2021, **11**, 36230–36236.

21 M. Chen, Z. Long, R. Dong, L. Wang, J. Zhang, S. Li, X. Zhao, X. Hou, H. Shao and X. Jiang, *Small*, 2020, **16**, 1906240.

22 M. Nakhaei, K. Akhbari, M. Kalati and A. Phuruangrat, *Inorganica Chim. Acta*, 2021, **522**, 120353.

23 Z. Zeng, J. Lyu, P. Bai and X. Guo, *Ind. Eng. Chem. Res.*, 2018, **57**, 9200–9209.

24 J. Winarta, B. Shan, S. M. Mcintyre, L. Ye, C. Wang, J. Liu and B. Mu, *Cryst. Growth Des.*, 2020, **20**, 1347–1362.

25 F. Ahmadijokani, R. Mohammadkhani, S. Ahmadipouya, A. Shokrgozar, M. Rezakazemi, H. Molavi, T. M. Aminabhavi and M. Arjmand, *Chem. Eng. J.*, 2020, **399**, 125346.

26 L. Hang, F. Zhou, D. Men, H. Li, X. Li, H. Zhang, G. Liu, W. Cai, C. Li and Y. Li, *Nano Res.*, 2017, **10**, 2257–2270.

27 S. Singh, P. K. Singh, A. Umar, P. Lohia, H. Albargi, L. Castañeda and D. K. Dwivedi, *Micromachines*, 2020, **11**, 779.

28 R. Abazari, A. R. Mahjoub and J. Shariati, *J. Hazard. Mater.*, 2019, **366**, 439–451.

29 N. Mudgal, P. Yupapin, J. Ali and G. Singh, *Plasmonics*, 2020, **15**, 1221–1229.

30 Z. Samavati, A. Samavati, A. Fauzi Ismail, N. Yahya, M. A. Rahman and M. Hafiz Dzarfan Othman, *Opt. Laser Technol.*, 2021, **136**, 106722.

31 Y. Huang, C. Tao, R. Chen, L. Sheng and J. Wang, *Nanomaterials*, 2018, **8**, 676.

32 M. B. Hossain, I. M. Mehedi, M. Moznuzzaman, L. F. Abdulrazak and M. A. Hossain, *Results Phys.*, 2019, **15**, 102719.

33 T. Khampieng, V. Yamassatien, P. Ekabutr, P. Pavasant and P. Supaphol, *Adv. Polym. Technol.*, 2018, **37**, 2030–2042.

34 K. Zhou, J. Chen, T. Wang, Y. Su, L. Qiao and Y. Yan, *Appl. Surf. Sci.*, 2020, **520**, 146354.

35 S. Karoui, R. Ben Arfi, K. Mougin, A. Ghorbal, A. A. Assadi and A. Amrane, *J. Hazard. Mater.*, 2020, **387**, 121675.

36 S. Agarwal, P. Giri, Y. K. Prajapati and P. Chakrabarti, *IEEE Sens. J.*, 2016, **16**, 8865–8873.

37 A. Karczmarczyk, M. Dubiak-Szepietowska, M. Vorobii, C. Rodriguez-Emmenegger, J. Dostálek and K.-H. Feller, *Biosens. Bioelectron.*, 2016, **81**, 159–165.

38 H. Wu, S. Wang, S. F. Y. Li, Q. Bao and Q. Xu, *Anal. Bioanal. Chem.*, 2020, **412**, 7525–

7533.

39 S. Akgönüllü, H. Yavuz and A. Denizli, *Talanta*, 2020, **219**, 121219.

40 Z. Gu, L. Chen, B. Duan, Q. Luo, J. Liu and C. Duan, *Chem. Commun.*, 2016, **52**, 116–119.

41 D. E. Mustafa, T. Yang, Z. Xuan, S. Chen, H. Tu and A. Zhang, *Plasmonics*, 2010, **5**, 221–231.

42 M. J. Kwon, J. Lee, A. W. Wark and H. J. Lee, *Anal. Chem.*, 2012, **84**, 1702–1707.

43 K. Na, K. M. Choi, O. M. Yaghi and G. A. Somorjai, *Nano Lett.*, 2014, **14**, 5979–5983.

44 G. Gumilar, Y. V. Kaneti, J. Henzie, S. Chatterjee, J. Na, B. Yuliarto, N. Nugraha, A. Patah, A. Bhaumik and Y. Yamauchi, *Chem. Sci.*, 2020, **11**, 3644–3655.

45 J.-H. Lee, K. J. Gibson, G. Chen and Y. Weizmann, *Nat. Commun.*, 2015, **6**, 7571.

46 A. Sánchez-Iglesias, N. Winckelmans, T. Altantzis, S. Bals, M. Grzelczak and L. M. Liz-Marzán, *J. Am. Chem. Soc.*, 2017, **139**, 107–110.

47 J. Spreadborough and J. W. Christian, *J. Sci. Instrum.*, 1959, **36**, 116–118.

48 R. Fang, A. Dhakshinamoorthy, Y. Li and H. Garcia, *Chem. Soc. Rev.*, 2020, **49**, 3638–3687.

49 G. Li, S. Zhao, Y. Zhang and Z. Tang, *Adv. Mater.*, 2018, **30**, 1800702.

50 S. Mourdikoudis, R. M. Pallares and N. T. K. Thanh, *Nanoscale*, 2018, **10**, 12871–12934.

51 X. Liu, D. Li, X. Sun, Z. Li, H. Song, H. Jiang and Y. Chen, *Sci. Rep.*, 2015, **5**, 12555.

52 S. Eustis and M. A. El-Sayed, *J. Appl. Phys.*, 2006, **100**, 44324.

53 J. Lin, W. Zhou, A. Kumbhar, J. Wiemann, J. Fang, E. E. Carpenter and C. J. O'Connor, *J. Solid State Chem.*, 2001, **159**, 26–31.

54 Á. Martínez, Y. Lyu, F. Mancin and P. Scrimin, *Nanomaterials*, 2019, **9**, 622.

55 P. Q. T. Do, V. T. Huong, N. T. T. Phuong, T.-H. Nguyen, H. K. T. Ta, H. Ju, T. B. Phan, V.-D. Phung, K. T. L. Trinh and N. H. T. Tran, *RSC Adv.*, 2020, **10**, 30858–30869.

56 X. H. Vu, N. D. Dien, T. T. Ha Pham, N. Van Truong, N. X. Ca and V. Van Thu, *RSC Adv.*, 2021, **11**, 14596–14606.

57 S. Øien, D. Wragg, H. Reinsch, S. Svelle, S. Bordiga, C. Lamberti and K. P. Lillerud, *Cryst. Growth Des.*, 2014, **14**, 5370–5372.

58 K. M. Koczkur, S. Mourdikoudis, L. Polavarapu and S. E. Skrabalak, *Dalton Trans.*, 2015, **44**, 17883–17905.

59 J. H. Cavka, S. Jakobsen, U. Olsbye, N. Guillou, C. Lamberti, S. Bordiga and K. P. Lillerud, *J. Am. Chem. Soc.*, 2008, **130**, 13850–13851.

60 S. Mustapha, J. O. Tijani, M. M. Ndamitso, A. S. Abdulkareem, D. T. Shuaib, A. T. Amigun and H. L. Abubakar, *Int. Nano Lett.*, 2021, 11, 241-261.

61 J. I. Langford and A. J. C. Wilson, *J. Appl. Crystallogr.*, 1978, **11**, 102–113.

62 R. Xu, Q. Ji, P. Zhao, M. Jian, C. Xiang, C. Hu, G. Zhang, C. Tang, R. Liu, X. Zhang and J. Qu, *J. Mater. Chem. A*, 2020, **8**, 7870–7879.

63 G. Lu, C. Cui, W. Zhang, Y. Liu and F. Huo, *Chem. – An Asian J.*, 2013, **8**, 69–72.

64 M. J. Katz, Z. J. Brown, Y. J. Colón, P. W. Siu, K. A. Scheidt, R. Q. Snurr, J. T. Hupp and O. K. Farha, *Chem. Commun.*, 2013, **49**, 9449–9451.

65 Z. U. Zango, N. S. Sambudi, K. Jumbri, N. H. H. Abu Bakar, N. A. F. Abdullah, E.-S. M. Negim and B. Saad, *Chem. Eng. Sci.*, 2020, **220**, 115608.

66 X. Song, P. Yang, D. Wu, P. Zhao, X. Zhao, L. Yang and Y. Zhou, *Chem. Phys.*, 2020, **531**, 110655.

67 C. L. Luu, T. T. Van Nguyen, T. Nguyen and T. C. Hoang, *Adv. Nat. Sci. Nanosci. Nanotechnol.*, 2015, **6**, 25004.

68 T. M. Tovar, I. Iordanov, D. F. Sava Gallis and J. B. DeCoste, *Chem. – A Eur. J.*, 2018, **24**, 1931–1937.

69 S. Wang, Y. Yu, J. Yu, T. Wang, P. Wang, Y. Li, X. Zhang, L. Zhang, Z. Hu, J. Chen, Y. Fu and W. Qi, *Nanotechnology*, 2020, **31**, 255604.

70 M. Gu, M. Wu, S.-C. Wang, C. Chen, D. Xiong and F.-Y. Yi, *Electrochim. Acta*, 2020, **343**, 135617.

71 T. Yang, Q. Xiang, L. Feng, C. Dong, X. Zhang, Z. Ning, X. Lai and D. Gao, *J. Lumin.*, 2019, **214**, 116567.

72 H. Li, F. Meng, S. Zhang, L. Wang, M. Li, L. Ma, W. Zhang, W. Zhang, Z. Yang, T. Wu, S. Lee, F. Huo and J. Lu, *Angew. Chem. Int. Ed.*, 2020, **59**, 2457–2464.

73 A. M. M. Vargas, A. L. Cazetta, M. H. Kunita, T. L. Silva and V. C. Almeida, *Chem. Eng. J.*, 2011, **168**, 722–730.

74 M. A. Ahmad, N. Ahmad and O. S. Bello, *Appl. Water Sci.*, 2015, **5**, 407–423.

75 D. Li, J. Wu, P. Wu, Y. Lin, Y. Sun, R. Zhu, J. Yang and K. Xu, *Sens. Actuators B*, 2015, **213**, 295–304.

76 W. W. Lam, L. H. Chu, C. L. Wong and Y. T. Zhang, *Sens. Actuators B*, 2005, **105**, 138–143.

77 L. Kumar, R. Gupta, D. Thakar, V. Vibhu and S. Annapoorni, *Plasmonics*, 2013, **8**, 487–

494.

78 X. Yang, Y. Yuan, Z. Dai, F. Liu and J. Huang, *Sens. Actuators B*, 2016, **237**, 150–158.

79 H. Yu, Y. Chong, P. Zhang, J. Ma and D. Li, *Talanta*, 2020, **219**, 121324.

80 J. Shankwitz, D. Speed, D. Sinanan and G. Szulczewski, *Inorganics* , 2021, 9.

81 K. Ilaslan, I. H. Boyaci and A. Topcu, *Food Control*, 2015, **48**, 56–61.

82 P. Bock and N. Gierlinger, *J. Raman Spectrosc.*, 2019, **50**, 778–792.

83 J. Shao, M. Lin, Y. Li, X. Li, J. Liu, J. Liang and H. Yao, *PLoS One*, 2012, **7**, e48127.

84 R. F. Dias, C. C. da Costa, T. M. Manhabosco, A. B. de Oliveira, M. J. S. Matos, J. S. Soares and R. J. C. Batista, *Chem. Phys. Lett.*, 2019, **714**, 172–177.

85 S. Nizamov and V. M. Mirsky, *Biosens. Bioelectron.*, 2011, **28**, 263–269.

86 V. T. Hoang, G. Stępniewski, K. H. Czarnecka, R. Kasztelanic, V. C. Long, K. D. Xuan, L. Shao, M. Śmietana and R. Buczyński, *Appl. Sci.*, 2019, **9**, 1145.

87 J. Jatschka, A. Dathe, A. Csáki, W. Fritzsche and O. Stranik, *Sens. Bio-Sensing Res.*, 2016, **7**, 62–70.

88 Y. Jing, R. Wang, Q. Wang, Z. Xiang, Z. Li, H. Gu and X. Wang, *Adv. Compos. Hybrid Mater.*, 2021, **4**, 885–905.

89 T. Xue, S. Yu, X. Zhang, X. Zhang, L. Wang, Q. Bao, C. Chen, W. Zheng and X. Cui, *Sci. Rep.*, 2016, **6**, 21254.

90 H. Xiong, Q. Shen and T.-B. Long, *Results Phys.*, 2020, **19**, 103683.

91 A. Göçenoğlu Sarıkaya, B. Osman, T. Çam and A. Denizli, *Sens. Actuators B*, 2017, **251**, 763–772.

92 Y. Tang, R. Mernaugh and X. Zeng, *Anal. Chem.*, 2006, **78**, 1841–1848.